EUROPEAN ORGANIZATION FOR NUCLEAR RESEARCH

CERN-EP/82-155
8 October 1982

AN EXPERIMENTAL STUDY OF LARGE-ANGLE ELASTIC SCATTERING OF CHARGED MESONS AND ANTIPROTONS ON PROTONS AT 20 AND 30 GeV/c INCIDENT MOMENTA

C. Baglin[1], R.B. Böck[2], K. Brobakken[2,5], L. Bugge[5], T. Buran[5], A. Buzzo[4], P.J. Carlson[2], L. Causton[6,a)], M. Coupland[6,b)], D.G. Davis[6], B.G. Duff[6], S. Ferroni[4], I. Kenyon-Gjerpe[2,5], V. Gracco[4], J.P. Guillaud[1], J. Haldorsen[2], J.D. Hansen[3], P. Helgaker[2], F.F. Heyman[6], D.C. Imrie[6], E.K. Johansson[2], K. Kirsebom[2,5], S. Kooijman[6,a)], R. Lowndes[6,c)], A. Lundby[2], G.J. Lush[6], M. Macri[2,4], R. Möllerud[2,3], J. Myrheim[2,3,5], M. Poulet[1], J. Tavernier[1], L. Rossi[4], A. Santroni[4], B. Schistad[5], G. Skjevling[5], S.O. Sørensen[5], M. Yvert[1].

Annecy (LAPP)[1] - CERN[2] - Copenhagen (Niels Bohr Institute)[3] - Genova[4] - Oslo[5] - University College London[6] Collaboration

ABSTRACT

A description is given of an experiment to study elastic scattering of $\pi^{\pm}$, $K^{\pm}$ and $\bar{p}$ on protons at c.m. scattering angles from 45° to 100° at the incident laboratory momenta 20 GeV/c and 30 GeV/c. The corresponding t range is from -6.2 $(GeV/c)^2$ to -28 $(GeV/c)^2$. There are no previous observations for these reactions in this t range. High intensity and large geometrical acceptance were required in order to measure the low cross sections. The experiment used a double arm spectrometer. MWPC's were used for reconstruction, and threshold and differential Cerenkov counters for identification. Scintillation counters, Cerenkov counters and a hadron calorimeter were used in the trigger. The trigger logic utilized specially designed matrices and a hard wired microprocessor. The π^-p elastic scattering cross sections follow approximately the dimensional counting rule from 3.5 GeV/c and up to 30 GeV/c. The cross sections decrease by seven orders of magnitude in this energy range. The data is compared to quark models. None of these models give a comprehensive description of the results. However, some modifications to these models improve their consistency with the data.

a) During the course of the experiment L. Causton and S. Kooijman received Science Research Council Studentships.

b) Presently at Birkbeck College, London, England.

c) Presently at Camtec Electronics Ltd. Buckland Rd., Leicester, England.

To be submitted to Nuclear Physics

1. INTRODUCTION

It is generally assumed that hadron-hadron scattering at large four momentum transfer is dominated by the short distance behaviour of the quark and gluon fields, characteristically different from the behaviour in the Regge exchange region. The bound state nature of the hadrons cannot be probed in the Regge region. However, it can be argued [1] that if the hadrons are bound states of a finite number of constituents, the Regge behaviour of the differential cross section for two-body hadron reactions, $s^{\alpha(t)}$, changes into a power behaviour, s^{-N}, when s and -t become large. This power behaviour is expected to occur sooner at large scattering angles. The Reggeon field theory can, however, not predict at what energies the power behaviour sets in. It is therefore an experimental question.

Hadron-hadron interactions have been extensively studied in the peripheral or Regge region. Data in the large angle region around 90^{o} in the c.m.s. is, however, scanty. In this region proton-proton elastic scattering has been measured for incident momenta up to 24 GeV/c [2], π on proton up to 12.7 GeV/c [3], and K on proton up to 6.2 GeV/c [4]. The differential cross sections behave in this region approximately as

$$\frac{d\sigma}{dt} \sim s^{-n+2} f(\cos\theta_{c.m.}),$$

with n ranging from 12 to 10 [5]. This simple counting rule is to be expected from dimensional arguments if the fundamental interaction is quark-quark scattering and if the quark-quark interaction is canonical scale invariant. n is then the number of valence quarks in the interacting hadrons.

The angular dependence $f(\cos\theta_{c.m.})$ is model dependent. To calculate f, one needs to know the constituent structure of the hadrons and the basic interactions.

Data on wide angle two-body hadron interactions has been lacking at high energies where these ideas can be tested. The interpretations of hadron-hadron inelastic collisions are beset with uncertainties due to the fragmentation functions and to the transverse momenta of the constituents.

At very high momentum transfers violations of the simple counting rules are expected because of QCD corrections. Scaling violations have been measured

in deep inelastic lepton-hadron scattering. These scale breaking effects are, however, also caused by the bound state nature of the nucleon and by the production of heavy quarks.

We have performed an experiment at the CERN Super Proton Synchrotron (SPS) to study two-body hadron-hadron reactions at high energies and large scattering angles. The experiment was optimized for elastic scattering. Results on pion-proton and antiproton-proton elastic scattering have been presented as reports and publications [6].

Experimentally it is very difficult to measure these processes at high energies and large -t. Due to the small cross sections one has to manage high intensity beams and to have a very efficient rejection of the dominating background. The detectors were carefully designed to obtain good spatial resolution and to minimize time jitters. To reduce deadtime losses the trigger logic had a three-level structure and included specially designed matrix units and a fast processor. The signals from the multiwire proportional chambers were delayed on cables of twisted pairs until the event gate was present.

Two different geometrical layouts with acceptance in the medium -t region or in the large -t region have been used. We will describe the set up and discuss the results from the large -t and large angle set up.

Data were collected with both positive and negative beams at a momentum of 20 GeV/c and with negative beam at 30 GeV/c.

We present results on the following reactions:

$$\pi^{\pm} p \rightarrow \pi^{\pm} p$$
$$K^{\pm} p \rightarrow K^{\pm} p$$
$$\bar{p}p \rightarrow \bar{p}p$$
$$\bar{p}p \rightarrow \pi^{-}\pi^{+}$$
$$\bar{p}p \rightarrow K^{-}K^{+}$$

Some data on elastic pp reactions were collected for normalization purposes. In section 2 of this paper we discuss the experimental setup. The analysis of the data is discussed in section 3. In section 4 we present the results. The conclusions are found in section 5.

2. EXPERIMENTAL SETUP AND TECHNIQUES

2.1 General Features.

The experiment was located in the West Hall at the CERN Super Proton Synchrotron. The layout, shown in fig. 1, will be described in some detail in this section. The experimental techniques included multiwire proportional chambers (MWPC), scintillation and Cerenkov counters and a crude hadron calorimeter. The hydrogen target was placed at the upstream end of the spectrometer magnet. The two scattered particles were both momentum analyzed. The high intensity beam passed through the first MWPC's downstream of the target. The beam intensities varied between 10^7 and 5.10^7 ppb, with a burst length of about 1 s, repeated every 10 s.

2.2 Incident Beam and Beam Particle Detection.

The production target was 182 m upstream of the experimental target. It was struck by protons from the SPS with a maximum momentum of 200 GeV/c, producing a secondary beam with maximum momentum of 100 GeV/c. The downstream section of the incident beam is shown in fig. 2.

The beam was unseparated and contained π, K, p, e and μ. In order to reduce the electron contamination, a 4.6 mm thick lead absorber was placed in the beam at a vertical and horizontal focus. This reduced the electron content effectively to zero without appreciably increasing the divergence of the hadron beam at the target. The divergence at the vertex was required to be less than about 1.0 mrad. The beam fractions at 20 GeV/c and 30 GeV/c are given in table I.

The particle identification was given by three differential Cerenkov counters, CEDARs [7]. Two of the CEDARs were located upstream of the target and were set to count p and K. The third CEDAR was located downstream of the experimental target and was set to count K. Because of the high π rate, the CEDARs could not count πs effectively. The third CEDAR was necessary because at the highest intensities there was a finite probability that a π accompanied a K inside the CEDAR resolution time. If the π scattered, the event could be misidentified as a Kp event, since the threshold Cerenkov

counters C1 and C2 (see fig. 1) could not always distinguish effectively between a scattered π and K. This ambiguity was resolved when the third CEDAR counted the unscattered K.

The position and direction of the beam particle was determined by means of two beam hodoscopes, BH1 and BH2 in fig.2. They were located about 1 and 8 meters upstream of the target respectively. Each hodoscope consisted of 3 planes. Each plane was constructed from two rows of 20 scintillators each. The scintillator elements had dimensions $100 \times 5 \times 2.2$ mm^3. Each one was viewed by a photo multiplier (EMI 9826A) through a light guide. In order to resolve ambiguities, the three planes of a hodoscope were mounted with the scintillators vertical and at $\pm 45^0$ respectively.

The beam intensity was measured using the beam hodoscopes. An ionization chamber, located upstream of the CEDARs (fig.2) was used as a monitor, and was also used to correct for saturation effects of the phototubes of the beam hodoscopes. The hodoscopes were linear in intensity up to about $3 \cdot 10^7 s^{-1}$.

Four scintillation counters, SP3-6, were mounted around the beam upstream of the target. They counted the halo and constituted the beam veto counters. The target was a 1m long mylar cylinder of 4 cm radius, filled with liquid hydrogen. It extended partly inside the magnetic field.

2.3 Detection of the Scattered Particles.

The geometry accepted c.m. scattering angles from approximately 45^0 to 100^0 at 20 GeV/c and 30 GeV/c beam momentum. The corresponding range in -t is from 6.2 $(\text{GeV/c})^2$ to 28 $(\text{GeV/c})^2$. Typical acceptance distributions at 20 GeV/c are given in figures 12.

The spectrometer magnet had a field volume of about $1.50 \times 0.75 \times 1.50$ m^3. The current in the windings was 7 500 A, producing a vertical main field component of 1.56 T, and an $\int B\, dl$ of 2.34 T m.

The vertical inner walls of the magnet were covered with scintillation counters to veto inelastic events.

2.3.1 Threshold Cerenkov Counters.

The particle scattered into the left arm was identified by two Cerenkov counters, C1 and C2, and that in the right arm by the Cerenkov counters C3 and C4.

The main parameters of the different counters are summarized in table II. The different gas fillings were chosen to give appropriate thresholds. The Cerenkov light was focused onto photomultiplier tubes by spherical mirrors. This gave a rough space resolution which was used in the offline analysis. The tubes were fitted with Winston cones to increase the effective radius of the cathode from 10 to 16 cm. In order to increase the quantum efficiency of the photomultiplier tubes a thin layer of a wave length shifter, paraterphenyl, was evaporated onto the window. This, together with an increased cathode - first dynode voltage, increased the quantum efficiency by 60% for the RCA 8854 tube. For the 58 DVP tube the increase was even larger, a factor 2.2 [8]. Light-emitting diodes were mounted to the rim of each Winston cone. They were used for calibrating the ADC scale. More details on the optical system can be found in ref [9].

2.3.2 Multi-Wire Proportional Chambers.

The position measurements were provided by multi-wire proportional chambers. The chambers allowed for high particle fluxes with minimum dead time losses.

The left arm was equipped with 5 chamber modules (CH1, CH2, CH3, CH4, CH5), and the right arm with 4 chamber modules (CH1, CH2, CH3, CH6). Each module was constructed of from 3 up to 6 wire planes. Two of the planes in each module were rotated in order to reduce the number of ambiguities caused by multiple hits in the chambers. The angle of rotation was chosen to facilitate the online processor operations. Chamber CH5 was rotated 45° to maximize the geometrical acceptance.

Table III summarizes the properties of the different chambers. The large chambers, CH4, CH5 and CH6, have been described in detail elsewhere [10].

Great care had to be taken to ensure stable operation of the chambers. Ageing of MWPC's is caused by depositions on signal and HV electrodes. In the large chambers, CH4, CH5 and CH6 the cathode planes were made of graphite-coated, stretched mylar foils. During two years of operation essentially no ageing effects were observed in them.

In the large chambers the electrostatic attraction problem between HV electrodes and the anode plane was solved by placing suitably spaced-out corrugated kapton strips between the HV planes and the wire anode plane. A copper wire stretched along the kapton strip corrected for the dielectric effect from the strip.

It was important to ensure that the wires did not break during the course of operation. All chambers were therefore supplied with a safety system which rapidly disconected the H.V. supply when the current through a chamber rose above a preset limit.

CH2 was equipped with beam killers (flat kapton boxes surrounding that part of the wires exposed to the beam) to cut the rates on these wires.

The read-out electronics used for the chambers have been described in detail elsewhere [11].

The signals passed through 85 m long, twisted pair cables to the Receiver Memory Hybrid (RMH) modules. This delay of 450 ns was long enough to allow the trigger electronics to generate a gate which latched the signals into the memory registers.

2.3.3 Trigger Scintillation Counters.

The signals from the scintillator hodoscopes H1, H2, PH1 and PH2 (fig. 1) were, together with the veto counter signals, the input to the first level logic, forming the fast strobe.

The trigger scintillation hodoscopes had to cover a large geometrical acceptance and at the same time give a fast strobe with a minimum of time jitter. The hodoscopes were made with a polar coordinate structure to facilitate the

trigger logic which used the kinematical correlations between the secondary particles (figures 3 and 5). The trigger required, within the resolution of the counters, the two secondary tracks to be coplanar with the beam and to have the correct opening angle.

The jitter of the fast strobe was minimized by the special design of the PH1 and PH2 scintillator hodoscopes [12]. These Prompt Hodoscopes had a fast response, and the time resolution of an element in these hodoscopes was ~ 0.5 ns. Fig. 3 shows the pattern of scintillator elements which they contained. The elements had the dimensions 30 × 30 cm^2, 15 × 30 cm^2 and 15 × 15 cm^2, with the smallest elements closest to the beam. PH1 had 92 elements and PH2 82 elements. Fig. 4 describes the construction of one element. Each scintillator, 4 cm thick, was viewed by a photomultiplier on its axis on the downstream side. No light guide was used.

At the first level of the trigger logic the elements were OR'ed in rings, as shown in fig. 3. At the second level single elements were correlated.

The H1 and H2 sets of hodoscopes, just downstream of the magnet, were made of two scintillator planes, each 1 cm thick. The scintillators were constructed in the form of rings and wedges, as shown in fig. 5. The dimensions of the elements were given by the size of the target and the Prompt Hodoscope elements. H1 had 14 rings, each 5 cm wide, and H2 had 13 rings, each 8 cm wide. The rings were divided into an upper and a lower half with a photomultiplier (56AVP) at the external ends. There were 10 wedges in each hodoscope, all with a wedge angle of 15^0. The photomultipliers (56AVP) were mounted at the broad end of the counters.

2.3.4 Iron Calorimeters.

The trigger was dominated by low-energy secondaries. This background has both an electromagnetic and a hadronic part. To get rid of some of this background, two simple iron and scintillator sandwich calorimeters were used at the end of each arm.

The calorimeter in the left arm consisted of iron plates of dimension 200 × 200 × 10 cm^3, interspaced with scintillation counter planes. In the right arm, only a single scintillator plane behind 10 cm of iron was used. To

tolerate the high rates, the scintillator planes were made of an upper and a lower half. Each half consisted of elements with dimensions 100 × 12.5 × 2 cm^3. A photomultiplier (Philips 56 AVP or Philips 2232B) was mounted on each scintillator element.

In the trigger, the voltage amplitudes from all elements were summed and discriminated [14].

2.4 Trigger Logic and Data Acquisition.

The measurements were carried out using intense secondary beams, typically 5×10^7 particles per machine burst of approximately 1 second.

The trigger conditions utilized the kinematical constraints of elastic reactions. Within the resolution of the detectors, an event had to be coplanar, with an opening angle consistent with elastic kinematics. Signals from veto counters, Cerenkov counters and calorimeters were also inspected. The signals from the trigger counter planes were subject to multiplicity conditions. The large number of counter-element coincidences was arranged in specially designed coincidence matrices with ECL 10 000 series elements [13]. The rest of the logic was built from NIM modules.

In order to minimize the dead time, the trigger was organized into three main levels. Each level had a higher degree of sophistication and consequently a longer decision time. The time information was used only once, at the first level. The subsequent operations were in DC-logic.

The wiring diagram of the trigger logic is shown in fig. 6.

2.4.1 The Fast Logic, First Level.

This level produced a strobe signal used to latch the counter signals into CAMAC registers and the MWPC data into the Receiver Memory Hybrid (RMH) modules [11].

The various hodoscope signals were standardized and equalized in time. Elements in the Prompt Hodoscopes (PH) were OR'ed together into rings before

they entered 6 programmable fast matrix coincidence units (OR1, OR2, FM1-FM4). The logic did a rough test on the event geometry utilizing the constraints of elastic kinematics. Enabling or disabling of matrix nodes constituted the means of correlation. The matrices FM1-FM4 were programmed through CAMAC.

The correlations were between groups of elements in the hodoscopes:

PH1 * PH2 = OR1, OR2 (Up/Down, Down/Up)
PH1 * H1R = FM1
PH2 * H2R = FM2
H1R * H2R = FM3
H1W * H2W = FM4

Also included at this level were the beam veto counters, defining the beam region, and the magnet veto counters, which vetoed multibody events.

The fast strobe set a "strobe inhibit flip-flop." Further outputs from this level were inhibited for 300 ns, long enough for the next level to reach a decision.

The propagation delay through the fast matrices was 21 ns and the time resolution was less than 3 ns. The strobe rate was typically 1.3×10^4 per burst. The discriminators and the fast matrices were updating. There was therefore no contribution to the dead time from this level.

2.4.2 The Slow Logic, Second Level.

The second level performed a more accurate test on the event geometry by correlating the prompt hodoscopes on an element-to-element basis. Only combinations agreeing with the kinematics of elastic scattering were accepted. This was again done with matrix logic by two programmable 48 * 48 slow matrices (SM1, SM2).

The matrices operated on the trigger hodoscope data strobed into registers (Le Croy, LRS 2341). The registers were modified so that the register outputs were available on separate outputs as soon as the strobe pulse arrived.

The multiplicity logic required that the number of hits in the different hodoscope planes be limited to ≤ 2 in PH1, ≤ 1 in PH2, ≤ 2 in H1R and ≤ 2 in H2R. The multiplicity constraints introduced a substantial correction factor to the data, due to a high random veto. This correction is discussed in detail elsewhere [14].

The slow matrices and the multiplicity veto, together with the fast strobe, defined the "Geometry":

$$\text{"Geometry"} \equiv (\text{Fast strobe}) * (\text{'slow matrices'}) * (\overline{\text{Mult. veto}})$$

This level also used the signals from all the Cerenkov counters, and the calorimeter pulse heights were required to be above preset limits.

The second level generated the EVENT trigger, defined as follows:

π-EVENT: $C1 * C2 * (\overline{C3 * C4}) * \text{GEOMETRY} * \text{CALORIMETERS}$

K-EVENT: $\text{CEDAR2} * C2 * (\overline{C3 * C4}) * \text{GEOMETRY} * \text{CALORIMETERS}$

$\bar{p}$-EVENT: $\text{CEDAR1} * \text{GEOMETRY} * \text{CALORIMETERS}$

If the slow logic did not generate an EVENT trigger within 300 ns, the logic reset the CAMAC registers and the MWPC data in the RMH modules.

With an incident intensity of about 5×10^7 ppb, the EVENT trigger rate was about 110 per burst. There was therefore practically no contribution to the dead time from this level, either.

2.4.3 The Fast Processor, Third Level.

During the course of the experiment a third level utilizing a fast processor was introduced. It took advantage of the high spatial resolution of the MWPC's.

The data stored in the RMH modules were first clustered and renormalized in a special processor [15] before they were read into the hard-wired special-purpose processor. The processor reconstructed points and tracks in

the field-free region and calculated the coplanarity and the opening angle of the particle pair which produced the event trigger. For acceptable triggers, the processor generated an interrupt to the data acquisition computer. The processor processing times were between 60 and 250 μs, with an average of 130 μs, which is much shorter than the time needed for the data acquisition system to read the event data.

The processor rejected 55% of the EVENT-triggers. At an event rate of 120 per burst, the processor dead time losses were less than 5%.

The processor is described in detail elsewhere [16].

2.4.4 Data Acquisition System.

The on-line computer was a NORD-10 with 196K 16-bit words of memory. Peripheral equipment included 2 magnetic tape units and 9M bytes of disc system.

There were two main data acquisition paths from the detectors to the NORD-10. One was the standard CAMAC system used for storing and reading data from the CEDAR'S, Cerenkov counters, hodoscopes, etc. The other was the RMH system for collecting, storing and decoding of the MWPC data.
The 22 000 wires of the MWPC required fast read-out, and the RMH read-out system was especially designed for high speed read-out of MWPC data [11].

An average of about 400 words were read per event. The CAMAC and the RMH read-out time of 3.5-4 ms per event was the dominant contribution to the overall dead time. An event interrupt rate of 120 per second was accompanied by a dead time loss of 50%.

3. DATA ANALYSIS

The data analysis, data corrections and normalization procedures are described in ref. [17].

3.1 Pattern recognition and event reconstruction

Due to the large amount of data and the extremely small cross sections to be studied, it was particularly important to make the analysis programs efficient and accurate.

As the data sample was reduced the selection criteria were tightened and the reconstruction methods were more accurate.

The amount of MWPC data was reduced at an early stage in the pattern recognition by defining roads in the two arms. The fired elements in the H1, H2, PH1 and PH2 hodoscopes consistent with the correlations in the trigger, together with the target position, defined the roads. Only the wires of the MWPC's inside these roads were considered.

The track finding started in the field free region downstream of the magnet. Straight lines were fitted to the patterns of fired wires. The straight lines were extrapolated into the magnetic field using the simplest possible track model with five linear parameters.

The track finding in the field free region was comparatively simple. In the cases when tracks were found and reconstructed, 1.1 lines on the average were reconstructed in each arm in the field free region. These lines had on the average 1.5 extensions into the magnetic field. The first approximation to the momentum of a track was calculated, assuming the magnetic field to be homogeneous inside a box.

Next a first approximation to the vertex was calculated. The field was assumed to have cylindrical symmetry. The two tracks were extended, using mirror points of the measured ones, in a plane perpendicular to the track and through the symmetry axis of the field. A 2-prong vertex was reconstructed as the midpoint on the shortest distance between the two scattered tracks. This distance was required to be less than 3 cm.

All reconstructed beam tracks were then checked against the 2-prong vertices. The square of the distance from the 2-prong vertex perpendicular to the beam track was required to be less than 1 cm^2. A 3-prong vertex was defined to lie on this line 1/3 of the distance away from the 2-prong vertex.

The main selection criterion for elastic events, or antiproton annihilation events, was the χ^2 from a least squares fit [18] which involved both geometrical and kinematical constraints. One beam track and two outgoing tracks were required to meet at a common vertex, and to be consistent with the observed clusters in the MWPC's. In addition to these geometrical constraints, the four constraints of energy-and momentum conservation were imposed at the vertex. Because the beam track was not always observed in the beam hodoscopes, nominal values for the position and direction of the beam, with relatively large errors, were always used in this main fit. As the number if observed clusters varied, the number of degrees of freedom varied between 15 and 21.

When a beam track was measured, this information was included in a separate fit. In addition, for all events a purely geometrical fit was done, without the kinematical constraints, but using the measured beam track whenever this existed. Cuts were imposed on χ^2 from these two secondary fits, but these cuts influenced very little the final event sample.

3.2 Event Selection.

A total of 37.82 million triggers were accumulated and analyzed, 8.98 million triggers at 20 GeV/c with negative beam, 11.86 million triggers at 20 GeV/c with positive beam, and 16.98 million triggers at 30 GeV/c with negative beam.

77% of the collected data was rejected at an early stage in the analysis. 6% of these rejections were due to bad data, 62% were rejected because no tracks were recognized, and 9% had no acceptable vertex. The main reason for rejections in the pattern recognition was lack of digitizings.

The dominating background in the reconstructed sample consisted of events with a positive pion in the left arm, with momentum above the thresholds in C1 and C2, and a negative pion in the right arm, with momentum below the thresholds in C3 and C4. This charge combination could make an elastic trigger, because both particles were bent towards an opening angle simulating elastic geometry. This background was completely eliminated by selecting a positive track in the right arm and the track in the left arm to have the same sign as the beam. Between 2% and 5% of the reconstructed triggers met this criterion.

A reconstructed trigger had generally several possible event solutions. This was due to ambiguous tracking, particularly in the magnetic field. A line in the field free region gave on the average 1.5 extensions in the magnetic field region. On average, 1.6 vertices were reconstructed with acceptable vertex parameters when the tracks were combined. Cuts on χ^2 and the vertex parameters together with the Cerenkov signatures usually resolved these ambiguities.

Because of the limited beam track detection and reconstruction efficiency, the existence of a 3-prong vertex was not used as an acceptance criterion. Events without a reconstructed beam track were reconstructed using a nominal beam track. Whenever more than one beam track was reconstructed, the event candidates were tried fitted with all the measured beam tracks. Only the beam track giving the best fit was kept.

The vertex was reconstructed to a precision of a few millimeters in the beam (z) direction. The background from events with the vertex outside the target was therefore easy to get rid of. All triggers with at least one event with positive particles in both arms for positive beam and with a positive particle in the right arm and a negative particle in the left arm for negative beam were fitted, using geometrical and kinematical constraints. The triggers that contained at least one event with $\chi^2 < 500$ were then subject to the following selection criteria.

A. Cerenkov signatures.

The Cerenkov requirements as applied in the off-line analysis, were:

Event type	Requirements
$\pi p \to \pi p$	$C1 * C2 * \overline{C3} * \overline{C4}$
$Kp \to Kp$	$CEDAR2 * C2 * \overline{C3} * \overline{C4}$
$p(\bar{p})p \to p(\bar{p})p$	$CEDAR1 * \overline{C1} * \overline{C2} * \overline{C3} * \overline{C4}$
$\bar{p}p \to \pi^-\pi^+/K^-K^+$	CEDAR1

The Cerenkov requirements were applied to the photomultiplier tubes corresponding to the track position in the counters. Because of the gate length there was about 10% probability that CEDAR1 or CEDAR2 were fired simultaneously with a π trigger. All combinations of CEDAR signals were therefore allowed for π-induced events. For the same reason a CEDAR1 signal was allowed for the K trigger and a CEDAR2 signal was allowed for the $p(\bar{p})$ trigger.

B. Because of exceptional experimental conditions some data had to be rejected. Poor beam quality, and excess data in the readout of electronic elements and the MWPCs were the most frequent reasons for these rejections.

C. The vertex coordinates had to be within the target.

D. Triggers with 10 or more vertices were rejected.

E. A set of χ^2 cuts were imposed. First the χ^2 from the fit which utilized only the geometrical constraints had to be less than 40. Next the χ^2 from the fit with both geometrical and kinematical constraints was required to be less than 100, when a beam track was reconstructed. All events were finally fitted with a nominal beam particle. The χ^2 from this fit had to be less than 40.

F. Only one event was accepted for each trigger. If the pattern recognition was ambiguous the solution with the lowest χ^2 was selected.

The triggers which had event candidates with the properly selected charge combination of the secondary tracks and with $\chi^2 < 500$ are listed in table IV. The table shows how the samples of events were reduced when the selection criteria A to F were imposed.

The χ^2 distributions of the samples which remained before the final χ^2 cuts (pt.E above) and using a nominal beam particle are shown in figures 7, 8 and 9. The number of degrees of freedom varied between 15 and 21 due to the inefficiencies of the MWPC's. Only the event with the lowest χ^2 has been included in cases of ambiguities.

The χ^2 distributions are distorted because the errors were not correctly assigned. There was, however, no indication that the separation of signal from background could be improved by correcting the error estimates.

Strong elastic signals are seen in the distributions for πp and pp events. The numbers of events that passed the last χ^2 cuts are given in table IV. No $\bar{p}p$ events have been observed within the cuts. The trigger also allowed for two body annihilation events, $\bar{p}p \to \pi^-\pi^+$, K^-K^+. The analysis included these hypotheses. No events were observed.

3.3 Normalization

3.3.1 Corrections to the data.

The total beam flux was measured with the beam hodoscopes. The minor components, the $K^{\pm}$ and $p(\bar{p})$ fluxes, were measured with CEDAR1 and CEDAR2, respectively.

As discussed in chapter 2.2, the electrons were absorbed in a lead plate. The μ content was given by a Monte Carlo simulation of the beam. The $\pi^{\pm}$ fluxes could then be calculated. The beam composition is given in Table I.

When evaluating the cross sections it was necessary to know various corrections to the flux measurements and to the number of events. These correc-

tions fell in two groups. One group contained overall corrections which were valid for the whole sample of data. The other group of corrections depended on the varying experimental conditions, such as the beam intensity and the efficiencies of the equipment. These corrections were therefore monitored throughout the experiment. All corrections including those for detection efficiency and geometrical acceptance were applied as correction factors to the flux. We will first list the overall corrections of the first group.

(i) The measurement of the total flux gave a value 30% higher than the true flux. There were three reasons for this: geometrical overlap of hodoscope counter elements, δ-ray production, and interactions in the hodoscopes and in the CEDAR counters.

(ii) The absorption in the target reduced the effective flux by about 5%.

(iii) About 3% of the events were lost because of geometrical losses in the trigger hodescope planes, H's and PH's, due to small gaps between individual elements.

(iv) The statistical fluctuation in the pulseheights from the calorimeter gave a 5% to 10% loss. This loss was estimated by measuring the calorimeter efficiency as a function of momentum. Reconstructed secondary tracks were used for this purpose.

All these overall corrections were applied separately to the π,K and $p(\bar{p})$ cross sections. The other set of corrections were dependent on the beam intensity and on the variable efficiencies of the counters, the chambers and the trigger. To take into account the varying conditions, the data was split into periods with comparatively stable conditions. The corrections were calculated for each period separately. A recapitulation of these corrections with average or typical values is given below.

(i) Because of the high intensity, the beam hodoscope counting rate showed saturation effects. This was corrected for by comparing the hodoscope counting rate with the readings of the ionization chamber in the beam. The correction was given by the deviation from a linear relationship between these two measurements.

(ii) The multiplicity veto (MV) on the signals from the H's and PH's was part of the slow, second level logic (2.4.2), which generated the event signal. Imposing the multiplicity veto reduced the event rate to 1-5%. It gave, moreover, cleaner data, and a larger fraction of the recorded data became elastic events. However, the multiplicity veto generated random vetoing (RMV) of elastic events. This effect constituted by far the largest single correction factor to the data; it gave between 21% and 47% loss of events. It was therefore extremely important to understand the MV and RMV. Extensive studies have been done to this end [14].

The corrections to the cross sections from RMV were found by fitting the trigger reduction caused by the multiplicity veto to an exponential dependence, exp(kI), on the beam intensity I, as expected if the multiplicity vetoing were random. For elastic events this correction should disappear at low intensities. A multiplicity veto could, however, be caused by effects correlated to the event, such as δ-rays. The correlated effects have been estimated to be less than 10% [14].

In figure 10 is shown the measured relative reduction in trigger rate, R, due to the MV and RMV as a function of the beam intensity per burst, I, for a selected sample of data. Each entry point represents about 400 bursts.

R should be flat if the multiplicity veto only rejected a well defined fraction of the inelastic events. The drop in R with I is interpreted as due to increasing RMV with I. The random multiplicity veto was also measured by shifting the register gates out of time with the coincidence signals that created the gates. This could not be done during data-taking, however. The average loss of events from RMV was 38%.

(iii) The beam veto counters and the magnet veto counters (2.4.1) were part of the fast, first level logic. On average, these vetos reduced the strobe rate to 67%. The wedge counters (2.3.3) outside the acceptance were also used in veto, and reduced the strobe rate further down to about 20%, on average.

The random veto rate from these counters was measured by shifting the timing of the veto signals. The loss of events was measured to be between 1% and 6%. This agrees well with the single rates and signal widths of the veto signals.

(iv) The MWPC efficiencies were continuously monitored on-line. The chamber efficiencies were calculated off-line. No efficiency variations across the planes of the chambers were observed and each t-bin was weighted according to the efficiency of the chambers as a whole.

(v) Each photomultiplier of the threshold Cerenkov counters was monitored on-line with light emitting diodes (2.3.1). Off-line, the efficiency of C2 was found by comparing it with C1, which had higher threshold:

$$E(C2) = \frac{C1 * C2}{C1} \quad .$$

To find the efficiency of C1, pulseheight cuts were imposed on the signals from C2 before the comparison was made. For pions with momentum above 6 GeV/c, the overall efficiencies were typically: 97% for C1, 99% for C2, 96% for C3, and 92% for C4.

(vi) The livetime was given by the ratio between the gated and ungated beam hodoscope scalers. Some minor inefficiencies in the scalers were corrected for by fitting a continuous curve to the beam profile. The average livetimes were 0.63 at 20 GeV/c and 30 GeV/c with negative beams, and 0.65 at 20 GeV/c with positive beam.

(vii) The loss of events in the offline analysis was estimated to 15%.

The overall normalization was checked by analyzing a sample of data collected with elastic pp-trigger criteria. The result from this analysis is compared to previously published results at 19.3 GeV/c and 21.3 GeV/c [19] in figure 11. The agreement is good. The error in the normalization is estimated to ±15%.

3.3.2 Background in the analyzed data.

As discussed in 3.2, the most common background in the reconstructed data was due to inelastic reactions producing a positive pion in the left arm and a negative pion in the right arm. This background was eliminated by requiring a negative track in the left arm and a positive track in the right arm for negative beam, and positive tracks in both arms for positive beam. Among the events with correct charge combination there were several possible background

reactions due to quasi two-body nucleon resonance production with subsequent decay into a proton and a neutral pion. Production of the nucleon resonances with lowest masses gave events with configurations closest to that of elastic scattering. The χ^2 with only geometrical constraints will for such events be similar to that of elastic events. However, the χ^2 with both geometrical and kinematical constraints will be very different.

The contamination of the data from nucleon resonances was estimated by a Monte Carlo calculation. Δ (1232) quasi two-body production was generated with isotropic decay. The generated data was put through the analyzing programs. The χ^2 distribution of these events with elastic hypothesis was flat.

Comparing with the corresponding χ^2 distribution from elastically generated events implied that if the cross sections for all the N^* and Δ production taken together were equal to the elastic cross section, then nucleon resonance production gives a background in the elastic sample of less than 2%.

The background in the observed sample of events was finally estimated by a fit to the χ^2 distributions. A line through the origin was fitted to the observed number of events in each bin for $\chi^2 > 40$. The dotted lines in figures 7, 8 and 9 show the results of these fits. The estimated background is much smaller than the statistical errors, due to the small number of events.

The fitting procedure resulted in a clean separation of elastic and background events (3.2). The signals for $K^{\pm}p$ elastic scattering are, however, very weak. Four K^-p and two K^+p events were isolated at 20 Gev/c. It was verified that these events were not misidentified pion events. This would occur if there was an incident pion within the 17 ns resolution time of the kaon CEDAR counter and which scattered elastically and failed to produce a signal above the threshold in C1. The number of misidentified πp elastic events in the sample of Kp elastic events was estimated to be less than 0.1. Moreover, CEDAR3, which was at the downstream end of the experiment and tuned to kaons, did not register a count for any of the Kp events. The pulse heights of the signals from C2 were furthermore found to favour K rather than π for these events.

3.3.3 Acceptance.

Monte Carlo calculations were used to find the acceptance of the apparatus. The same method was used to set the correlation matrices in the trigger logic (2.4.1, 2.4.2). The incident momentum was given a random distribution with width equal to the momentum bite. The reaction point was also chosen at random within the target. Multiple scattering was taken into account when the particles were tracked through the apparatus. Acceptance curves for $\pi^{\pm}$p elastic scattering at 20 GeV/c are shown in figures 12.

4. RESULTS AND DISCUSSION

The differential cross sections, $\frac{d\sigma}{dt}$, as a function of the c. m. scattering angle are plotted in figures 13, 14, 15 and 16, and are listed in table V. The data from experiments at lower energies than the present are shown for comparison.

The energy dependences of the differential cross sections are very different in the medium and the large angle regions, and the structures at wide angles fade as the energy is increased. As argued in the introduction, these characteristics are expected if the hadrons are bound states of a finite number of constituents.

There are several models for the constituent structure of the hadrons and their interactions [20-26]. We have compared the constituent interchange model, CIM, [20, 24] to our data. The model assumes the fundamental interactions to be valence quark-quark scattering and that the quark-quark scattering is canonical scale invariant. Gluonic exchange is only internal to the hadronic wave functions.

According to this model the differential cross sections for meson proton scattering should behave as

$$\frac{d\sigma}{dt} = ({}^{\sigma_o}/_{s^8}) \quad f\ (\cos\theta_{cm}) \qquad (1)$$

when $s \to \infty$, $-t \to \infty$, and $-t/s \sim \cos\theta_{cm}$ is finite.

The CIM gives simple and definite predictions for the angular dependences of the cross sections at wide scattering angles:

$$
\begin{aligned}
f(\pi^+p) &= \frac{1+z}{(1-z)^4}\left(\frac{4\alpha}{(1+z)^2}+\beta\right)^2 \\
f(\pi^-p) &= \frac{1+z}{(1-z)^4}\left(\frac{4\beta}{(1+z)^2}+\alpha\right)^2 \\
f(K^-p) &= \frac{1+z}{(1-z)^4}\,\alpha^2 \qquad (2) \\
f(K^+p) &= \frac{1+z}{(1-z)^4}\,\frac{16\alpha^2}{(1+z)^4}
\end{aligned}
$$

where $z = \cos\theta_{cm}$, $\alpha = 2$ and $\beta = 1$. σ_o is the only free parameter and should be the same for $\pi^{\pm}p$ and $K^{\pm}p$ elastic scattering.

In ref. [6] we made a fit of the CIM to the $\pi^{\pm}p$ data at 20 and 30 GeV/c using the least squares method. Due to the limited number of events we have redone the fit using the maximum likelihood method assuming Poisson distributions. The results of these fits are given in table VIa. The results of the separate fits to the $\pi^{\pm}p$ cross sections at 20 and 30 GeV/c are shown in figures 17, 18.

Except for the π^-p data at 20 GeV/c the CIM as given above does not give a good description of the data.

The deficiency of the model is that its angular dependence is weaker than that of the observed differential cross sections. This is particular clear at 30 GeV/c. Moreover, the predictions for the K^-p differential cross sections from the fit to the $\pi^{\pm}p$ data are completely wrong. Four K^-p events were observed at 20 GeV/c and one K^-p event was observed at 30 GeV/c. The predictions are 0.16 and 0.17 respectively. The probabilities of this occuring assuming Poisson statistics are $2\cdot10^{-5}$ and 0.16, respectively. The K^+p cross sections are adequately described.

A better fit to the data is obtained when one of the assumptions of the CIM is relaxed. In the CIM, the differential cross sections are written in terms of two amplitudes, which can be expressed as known functions of energy

and scattering angle each multiplied by an integral which depends both upon $z(=\cos\theta_{cm})$ and the details of the quark wave functions. In the CIM the ratio of the integrals is set equal to unity.

If instead, it is assumed that the ratio of the integrals is equal to a free, real parameter γ:

$$f(\pi^+p) = \frac{1+z}{(1-z)^4}\left(\frac{4\alpha}{(1+z)^2} + \beta\gamma\right)^2$$

$$f(\pi^-p) = \frac{1+z}{(1-z)^4}\left(\frac{4\beta}{(1+z)^2} + \alpha\gamma\right)^2 \qquad (3)$$

$$f(K^-p) = \frac{1+z}{(1-z)^4}\,\alpha^2\gamma^2$$

$f(K^+p)$ is unaltered.

The result of the fit to the $\pi^{\pm}p$ data at 20 and 30 GeV/c of this modified form of the CIM are given in table VIb and shown in figures 17 and 18. The predicted $K^{\pm}p$ differential cross sections are shown in figures 19 and 20. The fit is good and the predictions for the K^-p cross sections are improved.

Another way of improving the CIM model is to introduce scale breaking effects. In QCD field theory scale invariance is not expected to hold exactly because of gluonic radiative corrections. QCD corrections to the dimensional counting rule have been calcualated [27]. The fixed angle elastic differential cross section for 2 body hadronic reactions is predicted to behave as:

$$\frac{d\sigma}{dt} \sim \left(\frac{\alpha_s(P_T^2)}{s}\right)^{n-2} \times \ell n\left(\frac{P_T^2}{\Lambda^2}\right)^{-2\Sigma\gamma_i} \times f(\cos\theta_{cm}) \qquad (4)$$

in the limit $s \to \infty$, $-t \to \infty$ and $-t/s$ finite.

$\alpha_s = 1/\ell n\left(\frac{P_T^2}{\Lambda^2}\right)$ is the running coupling constant where Λ^2 is the QCD scale parameter. The factor

$\ell n\left(\frac{P_T^2}{\Lambda^2}\right)^{-\Sigma\gamma_i}$, where γ_i are the anomalous dimensions, varies very slowly

with the transverse momentum, P_T, and has therefore been set to a constant value. The prediction for meson proton scattering is

$$\frac{d\sigma}{dt} = \sigma_o \left(\frac{\alpha_s(P_T^2)}{s} \right)^8 f(\cos\theta_{cm}), \qquad (5)$$

with σ_o and Λ as free parameters. We have assumed $f(\cos\theta_{cm})$'s as in (2).

The results of the fits of (5) to our data are given in table VIc and shown in figures 17, 18, 19 and 20. A definite improvement is observed for the fits to the π^-p differential cross sections. The fit to the π^+p data does not improve, nor does the fit to all the $\pi^{\pm}p$ data. The predictions for the $K^{\pm}p$ cross sections are shown in figures 19 and 20. The same remarks as for the unmodified CIM applies.

We have also fitted (5) to all the $\pi^{\pm}p$ data letting σ_o, Λ and n (from (4)) be free. The result is given in table VId. The fit is not good.

Fig. 21 shows the ratio of the K^- to π^- elastic differential cross sections integrated around 90^o in the c.m. as a function of the incident momentum. The dimensional counting rule predicts that this ratio should be constant at high energies. Experimentally, the ratio remains constant at about 0.5 between 5 and 12 GeV/c, but appears to increase at 20 GeV/c. The lines are model predictions as explained in the figure caption.

Fig. 22 shows the energy dependence of the K^-p cross section at $\cos\theta_{cm} \cong 0.3$. ($72^o$). The straight line represents the s^{-8} behaviour predicted by the dimensional counting rule. Within the errors the counting rule is obeyed from $s \sim 10$ GeV^2 to $s \sim 60$ GeV^2.

G. Preparata and J. Soffer have proposed a model to describe hadronic interactions at short distances [28]. They have recently published a fit of this model to the $\pi^{\pm}p$ elastic scattering data from the present experiment [28]. The cross sections given by their model vary more slowly with the c.m.s. scattering angle than that given by the CIM and the observed angular distributions for π^-p elastic scattering, definitly decrease faster with increasing scattering angle than that given by the model. The model predictions for the $K^{\pm}p$ elastic scattering cross sections are shown in figures 19 and 20 [28]. The observed K^-p cross sections are about a factor 10 larger than the predictions.

The model of Preparata and Soffer has an energy dependence of s^{-9} modulo log(s). We have in figure 23 plotted the cross sections for π^-p elastic scattering at 90^o in the c.m.s. from s = 5.6 GeV^2 (p_{lab}= 3.5 GeV/c) to s = 57.2 GeV^2 (p_{lab}= 30 GeV/c). It is not possible from this figure to distinguish between a s^{-8} and a s^{-9} dependence of the cross sections. We have previously published [6] the result of a fit of s^{-n} to our π^-p data together with data at 9.7/9.8 GeV/c [29]. For $\cos\theta_{c.m.s.} < 0.5$ we found $n \sim 9 \pm 0.5$ (Since this publication our π^-p data has been renormalized by + 36%.)

5. Conclusions

π^-p elastic scattering between 50^o and 90^o scattering angles in the c.m.s. follows approximately the dimensional counting rule from 3.5 GeV/c and up to 30 GeV/c. The cross sections decrease by approximately seven orders of magnitude in this energy range. The π^+p elastic scattering cross sections show the same behaviour up to 20 GeV/c. Very few $K^{\pm}p$ elastic scattering events were observed. The data show, within the statistical uncertainty, good agreement with the dimensional counting rule.

The ratio of the K^-p to the π^-p elastic scattering cross sections shows, however, a rise between 12 GeV/c and 20 GeV/c.

We have compared the data with the CIM quark model and with a quark model proposed by G. Preparata and J. Soffer [28]. The models do not give a comprehensive description of the observations. The measured K^-p elastic scattering cross sections are a factor 10 larger than the models predict. When some modifications are introduced to the CIM it gives an approximately correct description of the angular dependences of the cross sections. Using a QCD correction to the energy dependence a fit to the π^-p data at 20 GeV/c and 30 GeV/c gives 195 MeV for the cut off parameter Λ. A good description of the angular distributions is also obtained by setting the ratio of the two amplitudes in CIM equal to a free parameter.

We gratefully acknowledge the technical assitance of P. Anzoli, R.M. Audria, G. Barisone, S. Bianconi, G. Dromby, R. Kiesler, J.C. Lacotte, J.C. Lemarec, M. Morelli, B. Mouellic , F. Nordby, D. Ploujoux, P. Poggi, G. Solberg, R.H. Watson, D.B. Webb, the SPS experimental support group, the DD on-line support group, the EP electronics group, and the Danish Natural Science Research Council, IN2P3, CERN, Instituto Nationale di Fisica Nucleare, Norges Almenvitenskapelige Forskningsråd, United Kingdom Science and Engineering Research Council for their financial support.

TABLE I

Beam composition (%)*

Momentum (GeV/c)	π	K	p	μ
+ 20	81.8	2.8	9.3	6
- 20	89.6	2.2	2.1	6
- 30	88.6	3.1	2.2	6

* With lead absorber.

TABLE II

Main parameters for the threshold Čerenkov counters

		C1	C2	C3	C4
Radiator length (m)		4.6	3.4	1.9	2.6
Volume (m^3)		39	45	17	31
Number of mirrors		6	9	6	10
Mirror size (cm^2)		70×100	80×80	80×80	70×100
Gas filling, 20 GeV/c		N_2	Freon	Freon	CO_2
Gas filling, 30 GeV/c		He-N_2	Freon	Freon	Freon
Photomultiplier type		RCA8854	RCA8854	58DVP	RCA8854
Thresholds at 20 GeV/c	π	6.0	3.1	3.1	4.9
(GeV/c)	K	21.3	11.0	11.0	17.3
	p	40.5	20.8	20.8	33.0
Thresholds at 30 GeV/c	π	7.3	3.1	3.1	3.1
(GeV/c)	K	25.8	10.9	11.2	11.1
	p	49.0	20.9	20.7	20.7

TABLE III

Properties of the MWPC's

Ch.	Projections *)	Wire Spacings (mm)	Gas mixture
1	X,U,Y,V,X	1,2,2,2,1	81.4% Argon
			15.0% Isobutane
2	X,V,U	1,2,2	0.6% Freon
3	X,U,V,Y,X,X	2,2,2,2,2,2	3.0% Methylalcohol
4,5,6	X,V,Y,U	2,4,2,4	79.8% Argon
			19.2% CO_2
			0.8% Freon
			0.2% Isobutane

*) The U and V coordinates are at the angles -Arcsin (8/17) and +Arcsin (8/17) respectively, with respect to the horizontal X coordinate.

TABLE IV

Reduction of reconstructed event candidates.

20 GeV/c negative beam.

Number of event candidates with $\chi^2 < 500$: 4251. Corresponding number of triggers: 860.

Selection criteria		Event candidates remaining		
		πp	Kp	$\bar{p}p$
A.	Cerenkov signatures	387	59	52
B.	Bad data	341	54	21
C.	Vertex cut	121	16	13
D.	< 10 events/trigger	117	16	12
E.	χ^2 (geom.) < 40	108	14	9
	χ^2 (geom. + kin. with reconstr. beam) < 100	99	13	8
	χ^2 (geom. + kin. with nom. beam) < 40	39	4	0
F.	Ambiguities	38	4	0
	Finally accepted:	38	4	0

TABLE IV (contn'd)

20 GeV/c positive beam

Number of event candidates with $\chi^2 < 500$: 17758. Corresponding number of triggers: 6795.

Selection criteria		Event candidates remaining		
		πp	Kp	pp
A.	Cerenkov signatures	3023	1019	1498
B.	Bad data	2894	1000	1093
C.	Vertex cut	811	118	308
D.	< 10 events/trigger	805	112	305
E.	χ^2 (geom.) < 40	725	89	276
	χ^2 (geom. + kin. with reconstr. beam) < 100	678	88	260
	χ^2 (geom. + kin. with nom. beam) < 40	73	2	19
F.	Ambiguities	68	2	17
G.	Acceptance cut*	66	2	16
	Finally accepted:	66	2	16

* For all channels we required $-t > 6.2$ (GeV/c)^2. Below this value of $-t$ the acceptance calculations are uncertain. For pp-events we reqiure also that $-t < 12$ (GeV/c)^2.

TABLE IV (contn'd)

30 GeV/c negative beam.

Number of event candidates with $\chi^2 < 500$: 36811. Corresponding number of triggers: 4278.

Selection criteria		Event candidates remaining		
		πp	Kp	$\bar{p}p$
A.	Cerenkov signatures	3597	329	206
B.	Bad data	3377	269	40
C.	Vertex cut	653	15	2
D.	< 10 events/trigger	492	11	0
E.	χ^2 (geom.) < 40	388	9	0
	χ^2 (geom. + kin. with reconstr. beam) < 100	368	8	0
	χ^2 (geom. + kin. with nom. beam) < 40	36	1	0
F.	Ambiguities	26	1	0
	Finally accepted:	26	1	0

TABLE V

Differential cross sections

Reaction $\pi^- p$ at 20 GeV/c

$-t$ $((GeV/c)^2)$	Δt $((GeV/c)^2)$	$\cos\theta_{cm}$	$d\sigma/dt \times 10^{35}$ $(cm^2/(GeV/c)^2)$	error $\times 10^{35}$ *) $(cm^2/(GeV/c)^2)$
7.4	1.2	0.596	23.7	8.0
9.0	2.0	0.509	13.5	3.7
11.0	2.0	0.400	4.5	1.6
13.0	2.0	0.290	1.37	0.8
15.0	2.0	0.181	1.26	0.7
17.0	2.0	0.072	0.46	0.4
19.0	2.0	-0.037	0.83	upper limit
21.0	2.0	-0.146	1.79	upper limit

Reaction $K^- p$ at 20 GeV/c

$-t$ $((GeV/c)^2)$	Δt $((GeV/c)^2)$	$\cos\theta_{cm}$	$d\sigma/dt \times 10^{35}$ $(cm^2/(GeV/c)^2)$	error $\times 10^{35}$ *) $(cm^2/(GeV/c)^2)$
8.4	3.2	0.539	40.8	28.9
12.0	4.0	0.341	7.5	7.5
16.0	4.0	0.121	5.9	5.9

Reaction $\bar{p}p$ at 20 GeV/c

$-t$ $((GeV/c)^2)$	Δt $((GeV/c)^2)$	$\cos\theta_{cm}$	$d\sigma/dt \times 10^{35}$ $(cm^2/(GeV/c)^2)$	error
8.4	3.2	0.531	21.8	upper limit
12.0	4.0	0.331	8.0	upper limit
16.0	4.0	0.106	6.4	upper limit

TABLE V (contn'd)

Reaction $\pi^- p$ at 30 GeV/c

$-t$ $((GeV/c)^2)$	Δt $((GeV/c)^2)$	$\cos\theta_{cm}$	$d\sigma/dt \times 10^{36}$ $(cm^2/(GeV/c)^2)$	error$\times 10^{36}$ *) $(cm^2/(GeV/c)^2$
10.0	4.0	0.639	18.2	4.3
14.0	4.0	0.495	3.4	1.4
19.0	6.0	0.314	0.31	0.31
25.0	6.0	0.097	0.34	0.34

Reaction $K^- p$ at 30 GeV/c

$-t$ $((GeV/c)^2)$	Δt $((GeV/c)^2)$	$\cos\theta_{cm}$	$d\sigma/dt \times 10^{36}$ $(cm^2/(GeV/c)^2)$	error$\times 10^{36}$ *) $(cm^2/(GeV/c)^2)$
10.0	4.0	0.637	23.8	upper limit
14.0	4.0	0.492	13.1	- " -
19.0	6.0	0.311	7.5	7.5
25.0	6.0	0.094	6.2	upper limit

Reaction $\bar{p}p$ at 30 GeV/c

$-t$ $((GeV/c)^2)$	Δt $((GeV/c)^2)$	$\cos\theta_{cm}$	$d\sigma/dt \times 10^{36}$ $(cm^2/(GeV/c)^2)$	error
10.0	4.0	0.633	34.2	upper limit
14.0	4.0	0.487	18.1	upper limit
19.0	6.0	0.303	10.1	upper limit

TABLE V (contn'd)

Reaction $\pi^+ p$ at 20 GeV/c

$-t$ $((GeV/c)^2)$	Δt $((GeV/c)^2)$	$\cos\theta_{cm}$	$d\sigma/dt \times 10^{35}$ $(cm^2/(GeV/c)^2)$	error $\times 10^{35}$ *) $(cm^2/(GeV/c)^2)$
7.1	1.8	0.612	19.3	3.9
9.0	2.0	0.509	6.9	1.6
11.0	2.0	0.400	2.43	0.8
13.0	2.0	0.290	3.25	0.9
15.0	2.0	0.181	0.68	0.5
17.0	2.0	0.072	3.67	2.6

Reaction $K^+ p$ at 20 GeV/c

$-t$ $((GeV/c^2))$	Δt $((GeV/c)^2)$	$\cos\theta_{cm}$	$d\sigma/dt \times 10^{35}$ $(cm^2/(GeV/c)^2)$	error $\times 10^{35}$ *) $(cm^2/(GeV/c)^2)$
9.1	5.8	0.500	3.22	3.2
14.0	4.0	0.231	3.45	3.4

*) Errors are only the statistical ones.

TABLE VIa

Fit to CIM with 1 parameter (σ_o)

Data (GeV/c)	Number of ev.	$\sigma_o \times 10^{25}$ (cm^2 GeV^{14})	χ^2/Nb. dof.*)
$\pi^- p$ 20	38	$12.53^{+2.1}_{-1.9}$	1.04
$\pi^- p$ 30	26	$13.31^{+2.8}_{-2.4}$	2.57
$\pi^+ p$ 20	66	$6.53.^{+0.8}_{-0.6}$	1.57
$\pi^{\pm} p$ 20,30	130	$8.61^{+0.8}_{-0.7}$	1.89
$\pi^- p$ 20,30	64	$12.46^{+1.6}_{-1.5}$	1.47

*) A goodness of fit for the maximum likelihood method using Poisson distributions is not easily evaluated. χ^2 is taken from the least squares fit to the cross section distributions. The number of degrees of freedom is the number of bins less the number of parameters.

TABLE VIb

Fit to CIM with 2 parameters (σ_o,γ)

Data (GeV/c)	Number of dof.	$\sigma_o \times 10^{25}$ (cm^2 GeV^{14})	γ	χ^2/Nb. dof.
$\pi^{\pm}p$ 20,30	14	2.72±0.9	3.3±1.0	1.07

TABLE VIc

Fit to CIM with QCD correction to the s dependence

Data (GeV/c)	Number of dof.	$\sigma_o \times 10^{20}$ *) (cm^2 GeV^{14})	Λ *) (GeV)	χ^2/Nb.dof.
π^-p 20	4	11.97±2.0	0.325±0.014	0.5
π^-p 30	2	0.29±0.05	0.817±0.03	0.5
π^+p 20	4	66.1±8.6	0.152±0.007	1.3
π^-p 20,30	8	75.5±10.1	0.195±0.009	0.8

*) The parameters are strongly correlated in the fit. The errors given were found by varying one parameter at a time, keeping the others fixed, until χ^2 changed by 1.

TABLE VId**)

Fit to CIM with 3 parameters

Data (GeV/c)	Number of dof.	$\sigma_o \times 10^{23}$ (cm^2 GeV^{14})	Λ (GeV)	n	χ^2/N.dof.
$\pi^{\pm}p$					
	13	13.00±1.1	0.170±0.005	5.7±0.3	1.82
20,30					

**) The parameters were found by an iterative procedure. One parameter was kept fixed at a time. The errors were found as explained above (*).

References

1. D. Amati, L. Caneschi and M. Testa, CERN TH 1644 (1973)

2 J.V. Allaby et al., Nucl. Phys. B52 (1973) 316

3. P. Baillon et al., P.L. 94B (1980) 533
J. Chauveau. Thesis, Université Pierre et Marie Curie, Paris, 1981

4. T. Buran et al. Nucl. Phys., B111 (1976) 1

5. A. Lundby, Fifth Int. Conf. on High-Energy Collisions, Stony Brook, N.Y. USA, August 1973

6. R. Almås et al., EPS International Conference on High-Energy Physics, Geneva 1979
L. Bugge and T. Buran, Inst. of Phys., University of Oslo Report 80-07
R. Almås et al., P.L. 93B (1980) 199
Z. Asad et al., XX International Conference on High-Energy Physics, Madison 1980
Z. Asad et al., P.L. 108B (1982) 51

7. C. Bouvet et al., CERN/Lab. II/EA/74-4 (1975)

8. P.J. Carlson, NIM 158 (1979) 403

9. S. Kooijman. Thesis presented for the degree of Doctor of Philosophy in the University of London, March 1979

10. M. Bozzo et al., NIM 178 (1980) 77

11. J.B. Lindsay et al., NIM 156 (1978) 329

12. M. Poulet and A.Santroni, NIM 148 (1978) 359

13. R. Kiesler, EP-Electronics Note 80-04 (1980)

14. K. Kirsebom. Thesis submitted at the University of Oslo, 1981

15. L. Rossi, NIM 163 (1979) 71

16. I. Kenyon-Gjerpe. Thesis submitted at the University of Oslo, 1981

17. K. Brobakken, Thesis submitted at the University of Oslo, 1982

18. L. Bugge and J. Myrheim, NIM 179 (1981) 365

19. J.V. Allaby et al., P.L. 25B (1967) 156

20. R. Blankenbecler, S.J. Brodsky and J.F. Gunion, P.L. 39B (1972) 649
SLAC-PUB-2057 (1977)

21. D. Horn and M. Moshe, Nucl. Phys. B48 (1972) 557, Calt-68-382 (1973)

22. P.V. Landshoff, DAMTP 73/76, DAMTP 77/28

23. V.A. Matvev, R.M. Muradyan and A.N. Tankelidze, Lett. Nuovo Cimento 5, (1972) 907

24. S.J. Brodsky and G.R. Farrar, P.R.L. 31 (1973) 1153

25. D. Cline, F. Halzen anx M. Waldrop, Nucl. Phys. B55 (1973) 157

26. P. Fishbane and C. Quigg, Nucl. Phys. B61 (1973) 469

27. G.P. Lepage and S.J. Brodsky, SLAC-PUB-2478 (1980)

28. G. Preparata and J. Soffer, P.L. 86B (1979) 304, P.L. 92B (1980) 187

29. D.P. Owen et al., P.R. 181 (1969) 1794

30. Å. Eide et al., Nucl. Phys. B60 (1973) 173

31. C. Baglin et al., Nucl. Phys. B98 (1975) 365

32. A.W. Lowman and N.A. McCubbin, Nucl. Phys. B61 (1973) 296

33. A. Berglund et al., Nucl. Phys. B137 (1979) 276

34. R. Rubinstein et al., P.R.L. 30 (1973) 1010

35. F. Marzano et al., P.L. 68B (1977) 292

36. C.T. Coffin et al., P.R. 159 (1967) 1169

37. Sonderegger et al., XIX International Conference on High-Energy Physics, Tokyo 1978.

38. P. Cornillon et al., P.R.L. 30 (1973) 403.

Figure Captions

Fig. 1 The experimental layout. C_1, C_2, C_3 and C_4 are threshold Čerenkov counters, CEDAR3 is a differential Čerenkov counter. H, PH1 and PH2 are hodoscope trigger scintillation counters. CH1 to CH6 are modules of multiwire proportional chambers. Block 1 and 2 are crude hadron calorimeters.

Fig. 2 The layout of the downstream section of the beam. BH1 and BH2 are finger scintillation counters. SP3-6 are halo counters (to veto beam halo). Cedar 1 and Cedar 2 are differential Čerenkov counters.

Fig. 3 The pattern of prompt hodoscope elements as seen from downstream. At the first level of the trigger logic the single elements were ored as shown in this figure.

Fig. 4 Constructional details of a prompt hodoscope element. [12].

Fig. 5 The pattern of the H1 and H2 hodoscope elements as seen from upstream.

Fig. 6 The wiring diagram of the trigger logic. OR1, OR2, FM1 to FM4, SM1 and SM2 are defined in chapters 2.4.1 and 2.4.2. FO and Sh are fanouts and shapers.
Č1, Č2, Č3 and Č4 are the threshold Čerenkov counters. Cedar 1 and Cedar 2 are the differential Čerenkov counters. H1, H2, PH1 and PH2 are the trigger hodoscopes. H1 mult., H2 mult. PH1 mult. and PH2 mult. are multiplicity requirements on the trigger hodoscopes. RMH are the Receiver Memory Hybride moduls for reading and storing the multiwire proportional chamber signals. Nord is the online computer.

Fig. 7 χ^2 distributions of π^-p (a), K^-p (b) and $\bar{p}p$ (c) elastic event candidates at 20 GeV/c.

Fig. 8 χ^2 distributions of π^+p (a), K^+p (b) and pp (c) elastic event candidates at 20 GeV/c.

Fig. 9 χ^2 distributions of π^-p (a), K^-p (b) and $\bar{p}p$ (c) elastic event candidates at 30 GeV/c.

Fig. 10 The relative reduction in trigger rate, R, due to the multiplicity veto and the random multiplicity veto as a function of the beam intensity, I. The curve is discussed in the text (3.3.1).

Fig. 11 Differential cross sections of pp elastic scattering at 19.3 GeV/c and 21.3 GeV/c [19] and at 20 GeV/c measured in this experiment.

Fig. 12. Geometrical acceptance at 20 GeV/c for π^-p (a) and π^+p (b) elastic scattering.

Fig. 13. Differential cross sections of π^-p elastic scattering. Data at 20 GeV/c and 30 GeV/c are from this experiment. Data at other energies at 5.0 Gev/c [30], 6.2 GeV/c [4], 9.7/9.8 GeV/c [29], 12.7 GeV/c [3] and 22.6 GeV/c [38].

Fig. 14 Differential cross sections of π^+p elastic scattering. Data at 20 GeV/c is from this experiment. Data at 5 GeV/c and 10 GeV/c are from references [30] and [31] respectively.

Fig. 15 Differential cross sections of K^-p elastic scattering. Data at 20 GeV/c and 30 GeV/c are from this experiment. Data at 3.59 GeV/c, 5.0 GeV/c, 6.2 GeV/c, 10.1 GeV/c and 13.6 GeV/c are from references [32], [30], [4], [33] and [29] respectively.

Fig. 16 Differential cross sections of K^+p elastic scattering. Data at 20 GeV/c is from this experiment. Data at 5 GeV/c, 10 GeV/c and 13.8 GeV/c are from references [30], [31] and [34] respectively.

Fig. 17 Differential cross sections of π^-p elastic scattering at 20 GeV/c and 30 GeV/c measured in this experiment. The dashed curves are the results of a fit of the Constituent Interchange Model [20], the dashed/dotted lines are the results of a fit of a modified form of the CIM with 2 parameters and the continuous lines are the results of a fit with QCD corrections to the energy dependence in the CIM [27].

Fig. 18 Differential cross sections of π^+p elastic scattering at 20 GeV/c measured in this experiment. The curves are explained in figure 17.

Fig. 19 Differential cross sections of K^-p elastic scattering at 20 GeV/c and 30 GeV/c measured in this experiment. The curves are predictions from model fits to the $\pi^{\pm}p$ cross sections. See text.

Fig. 20 Differential cross sections of K^+p elastic scattering at 20 GeV/c measured in this experiment. The curves are predictions from model fits to the $\pi^{\pm}p$ cross sections. See text.

Fig. 21 The ratio of the K^-p to the π^-p elastic scattering cross sections integrated between the c.m.s. scattering angles from +0.5 to -0.5. Our measured cross sections for $\cos\theta_{c.m.s.} > 0$ have been extrapolated to $\cos\theta_{c.m.s.} < 0$ using the CIM. The data at 5. GeV/c, 6.2 GeV/c and 12. GeV/c are from references [30], [4] and [37] respectively. The data at 20 GeV/c is from this experiment.
The solid and dotted lines are the predictions of the CIM and the modified CIM(σ_0,γ). The dashed line is the prediction of the model of Preparata and Soffer [28].

Fig. 22 The energy dependence of the K^-p elastic differential cross sections at $\cos\theta_{c.m.s.} = 0.3$. The data at 20 GeV/c and 30 GeV/c are from this experiment. The other datapoints are at 3.6 GeV/c [32], 4.2 GeV/c [35], 5.0 GeV/c [30], 5.9 GeV/c [29] and 9.7 GeV/c [29] respectively.

Fig. 23 The energy dependence of the π^-p elastic differential cross sections at 90^o in the c.m.s. The data at 20 GeV/c and 30 GeV/c are from this experiment. The other datapoints are at 2.5 GeV/c [36], 3.0 GeV/c [36], 3.5 Gev/c [36], 5.0 GeV/c [30], 5.9 GeV/c [29], 6.2 GeV/c [4], 7.88 GeV/c [29], 9.84 GeV/c [29] and 11.9 GeV/c [3] respectively.

TB/gs/41 B

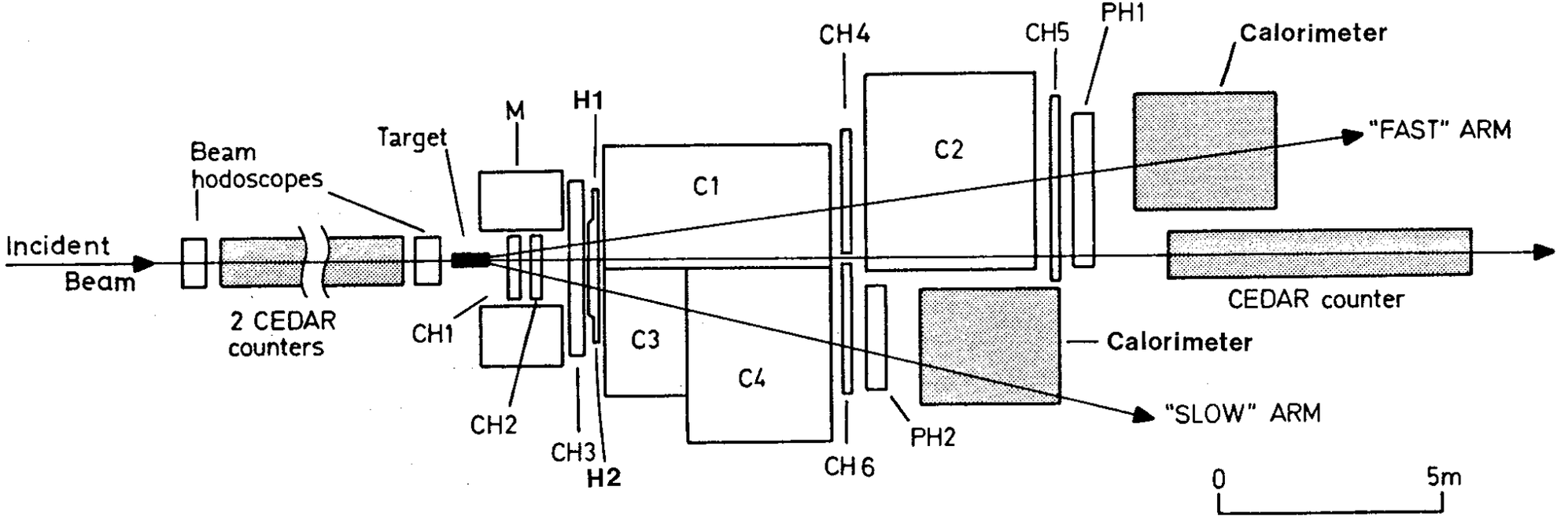
Incident
Beam
Beam
hodoscopes
2 CEDAR
counters
Target
M
H1
CH1
CH2
CH3
H2
C1
C2
C3
C4
CH4
CH5
CH6
PH1
PH2
Calorimeter
"FAST" ARM
CEDAR counter
Calorimeter
"SLOW" ARM
0
5m

Fig. 1

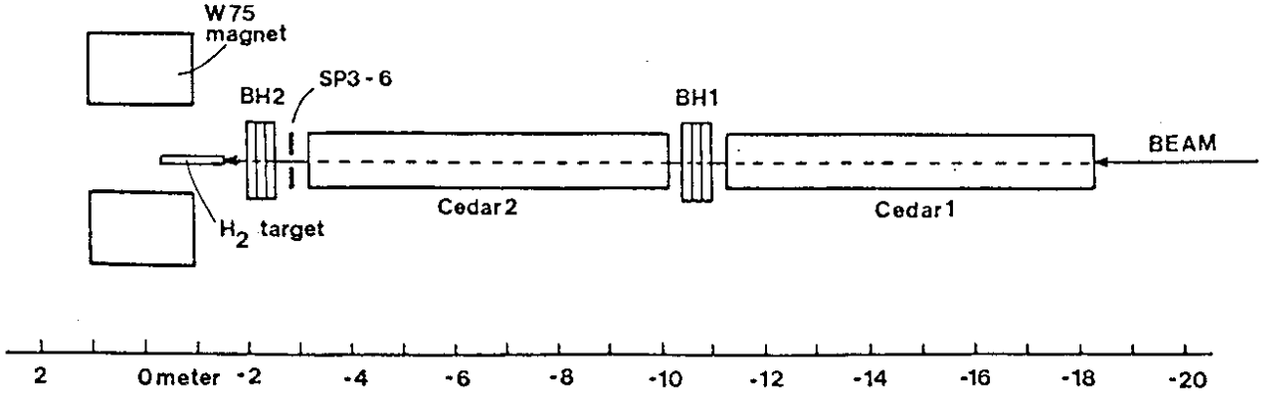
W75
magnet
BH2
SP3-6
BH1
BEAM
Cedar2
Cedar1
H_2 target
2
0meter
-2
-4
-6
-8
-10
-12
-14
-16
-18
-20

Fig. 2

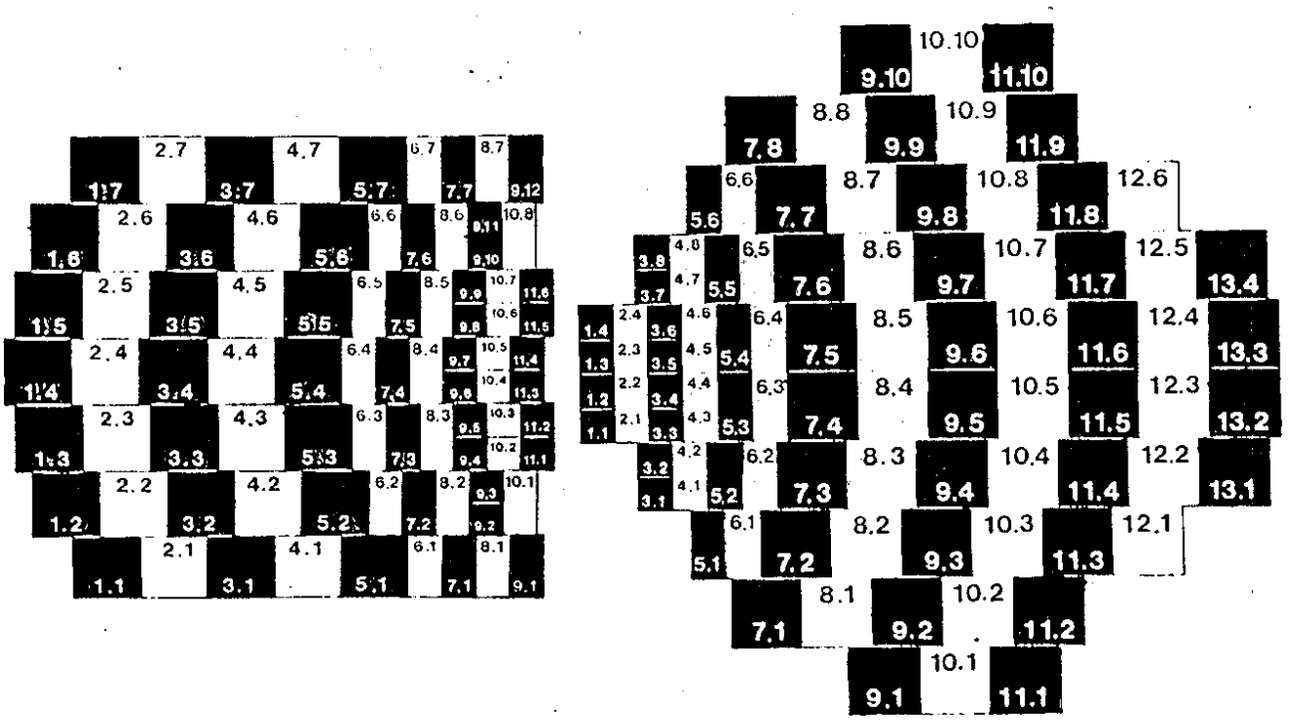

Fig. 3

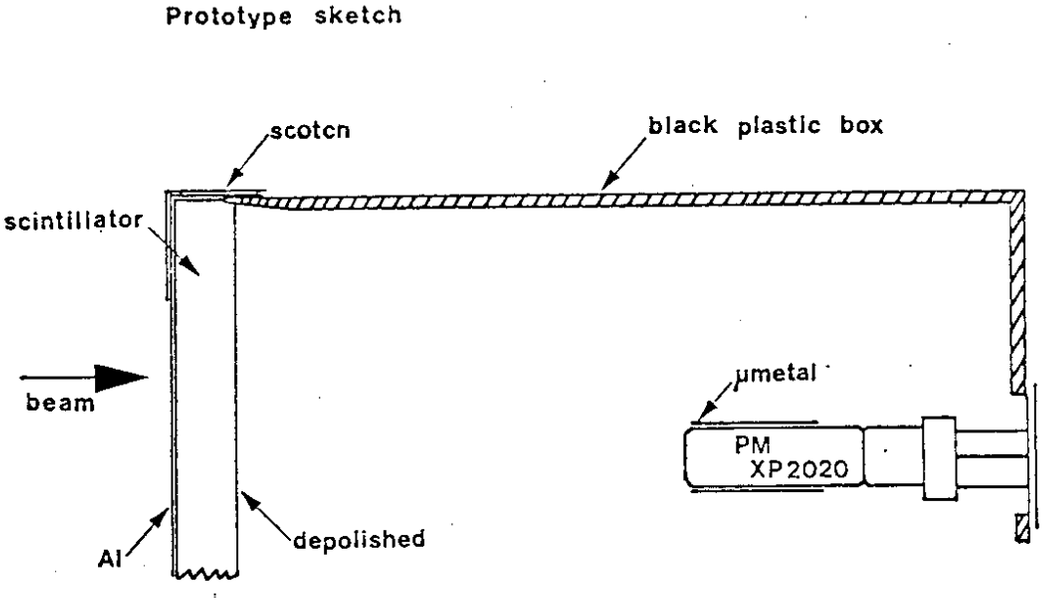
Prototype sketch
scotch
black plastic box
scintillator
beam
μmetal
PM
XP2020
Al
depolished

Fig. 4

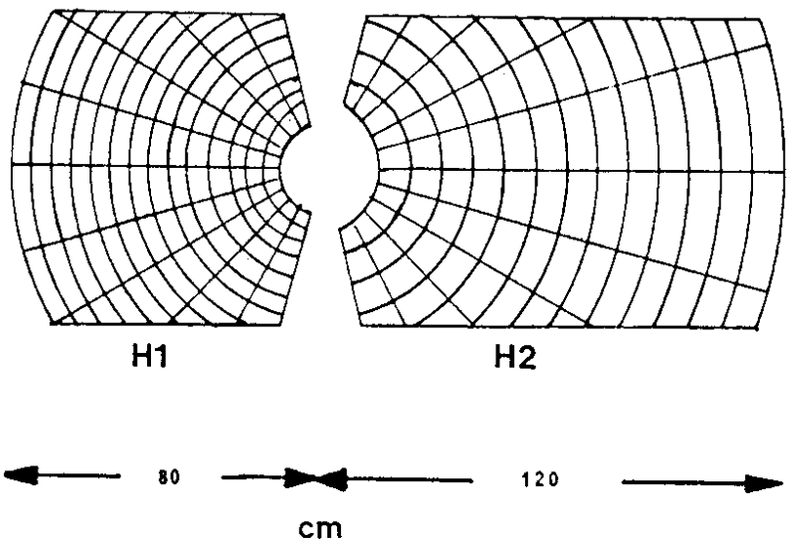

Fig. 5

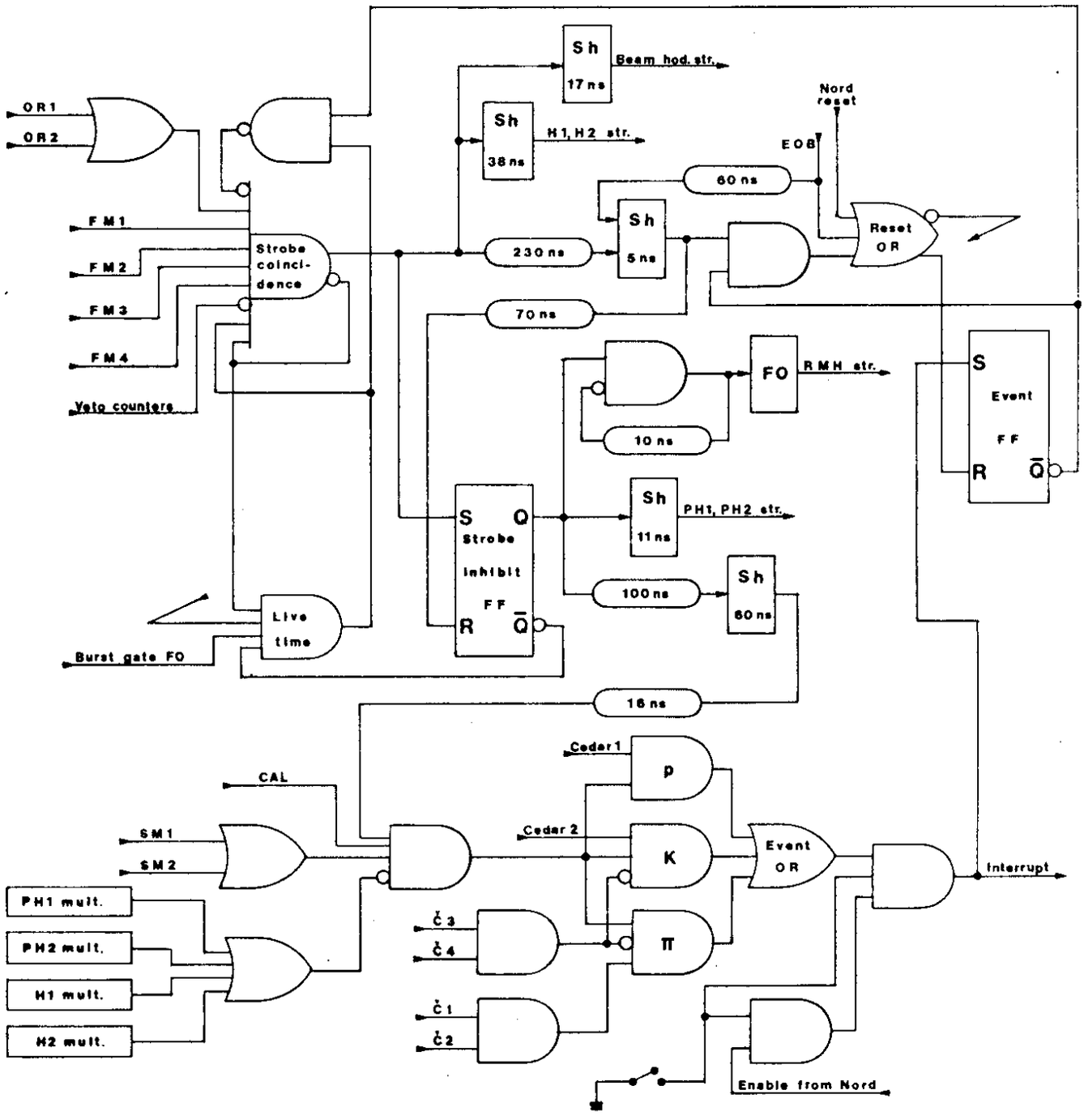
OR1
OR2
FM1
FM2
FM3
FM4
Veto counters
Strobe coinci-dence
Sh 17 ns
Beam hod. str.
Sh 38 ns
H1, H2 str.
Nord reset
EOB
60 ns
Sh 5 ns
230 ns
Reset OR
70 ns
FO
RMH str.
10 ns
S Event FF R Q̄
S Q Strobe inhibit FF R Q̄
Sh 11 ns
PH1, PH2 str.
100 ns
Sh 60 ns
Live time
Burst gate FO
16 ns
Ceder 1
p
CAL
SM1
SM2
Ceder 2
K
Event OR
Interrupt
PH1 mult.
PH2 mult.
H1 mult.
H2 mult.
C̄3
C̄4
π
C̄1
C̄2
Enable from Nord

Fig. 6

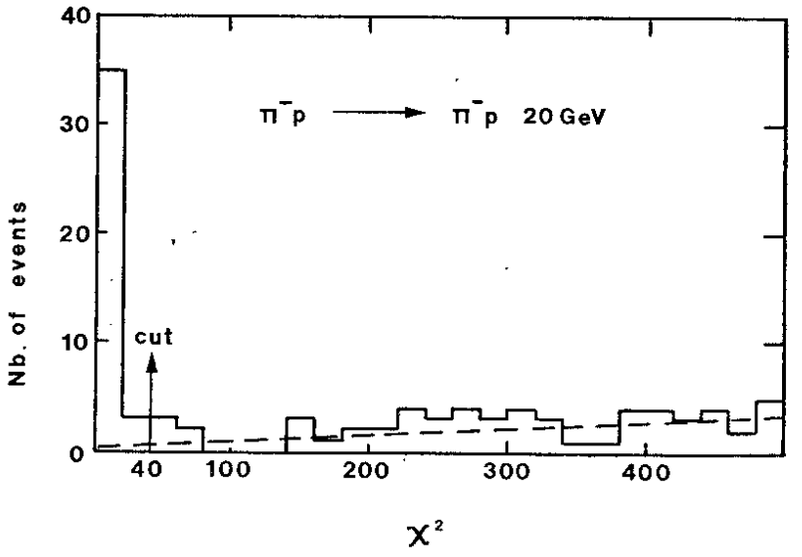

Fig. 7a

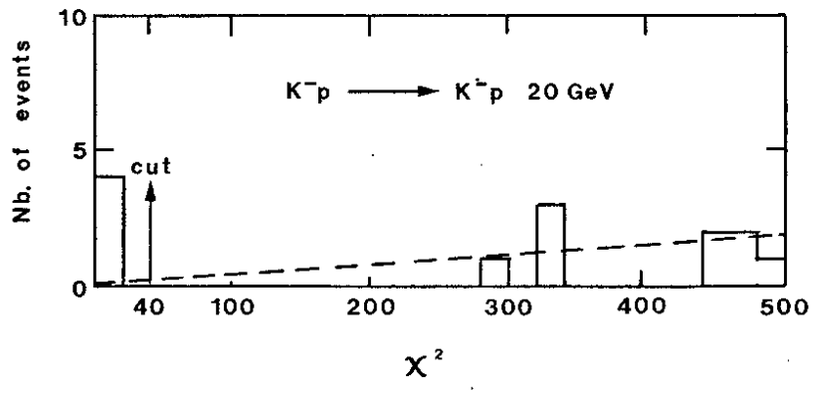

Fig. 7b

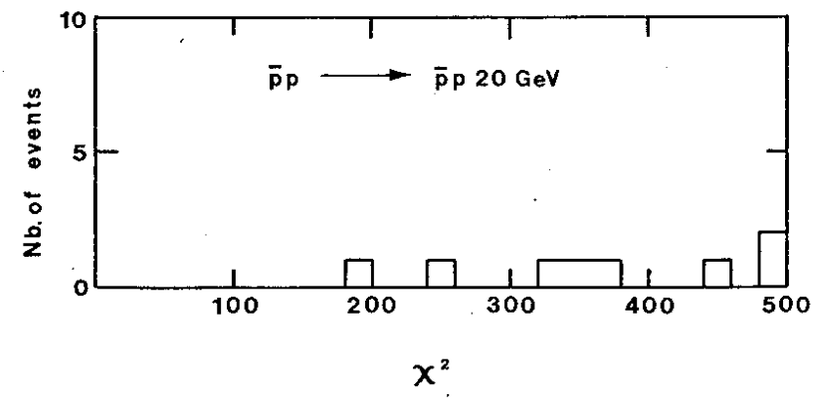

Fig. 7c

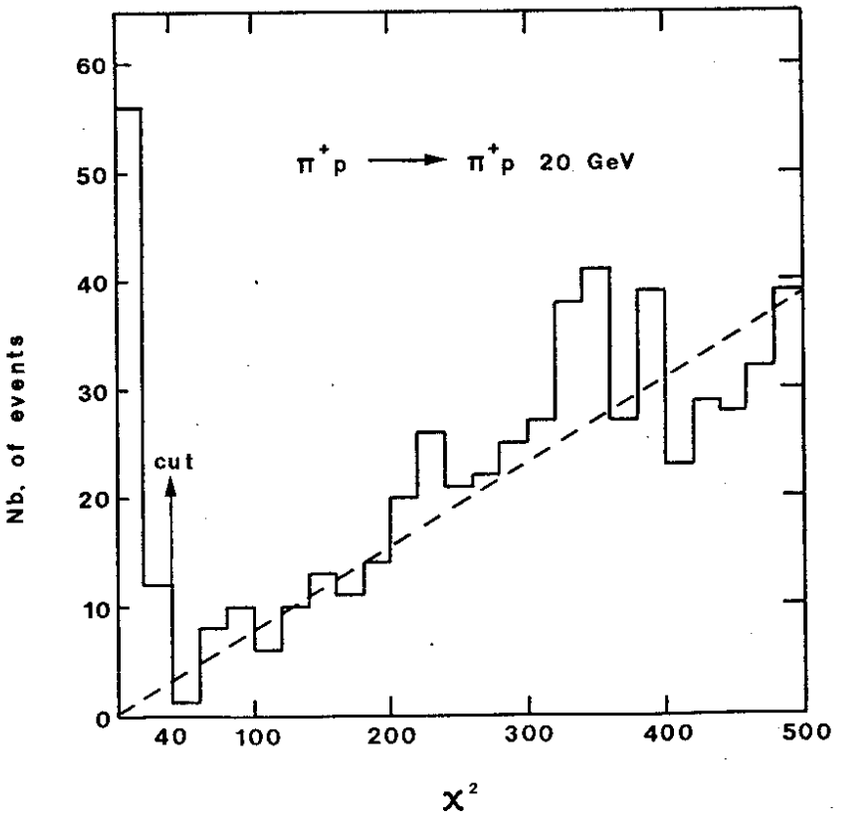
$\pi^+p \longrightarrow \pi^+p$ 20 GeV
Nb. of events
cut
60
50
40
30
20
10
0
40
100
200
300
400
500
χ^2

Fig. 8a

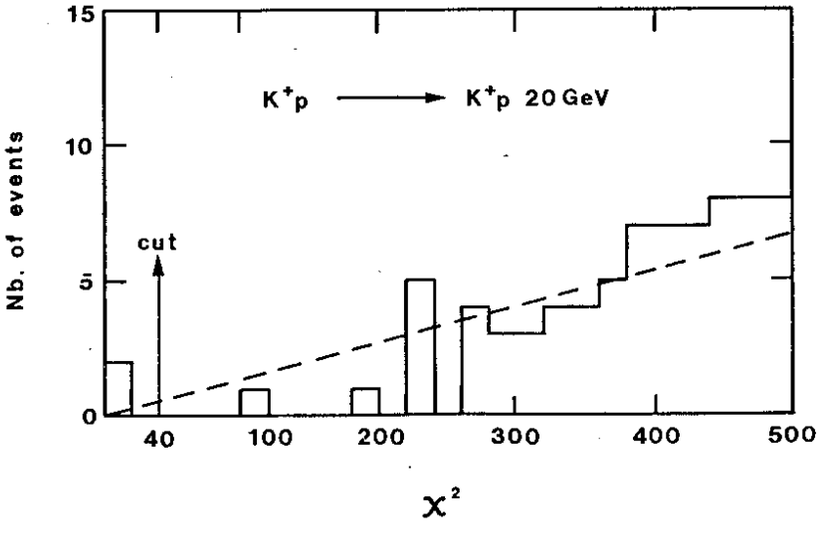
$K^+p \longrightarrow K^+p$ 20 GeV
Nb. of events
cut
15
10
5
0
40
100
200
300
400
500
χ^2

Fig. 8b

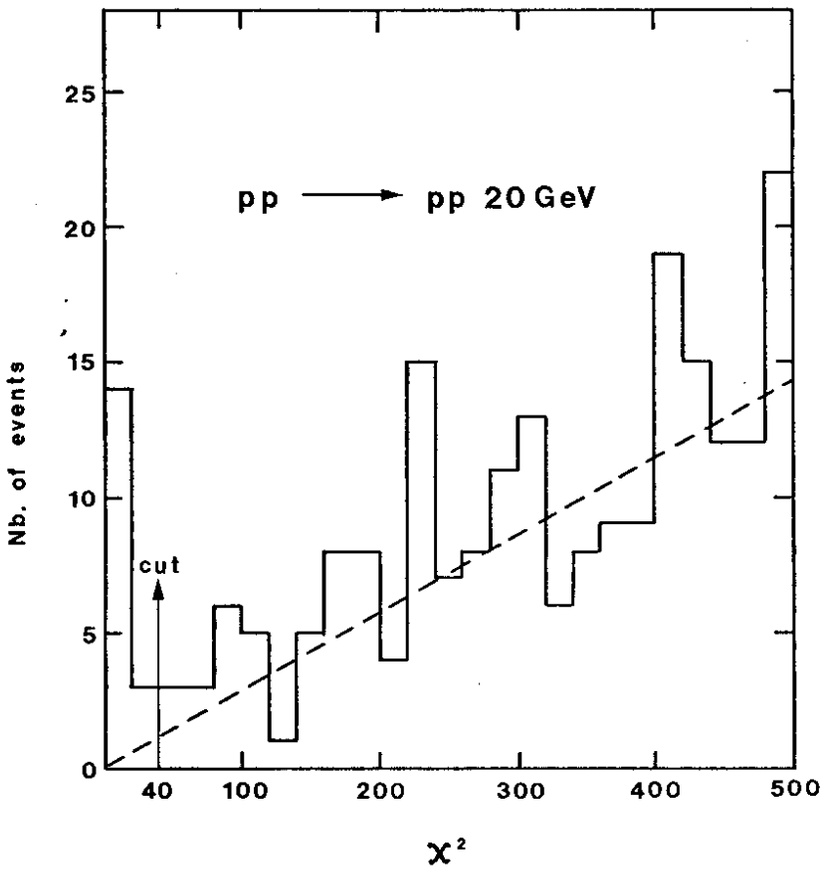
pp ⟶ pp 20 GeV
Nb. of events
cut
χ^2
0
5
10
15
20
25
40
100
200
300
400
500

Fig. 8c

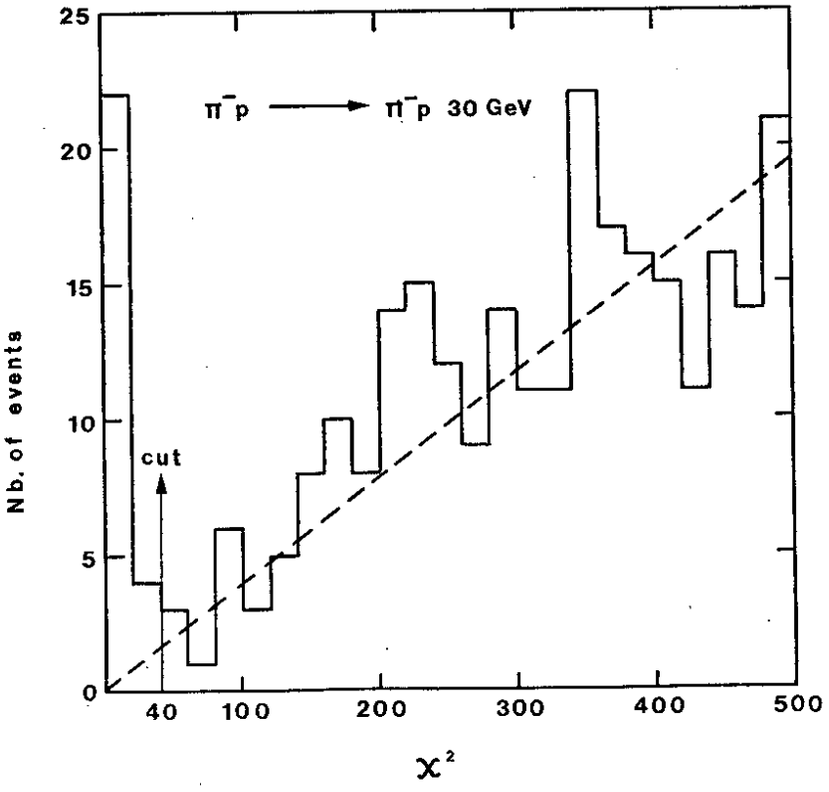

Fig. 9a

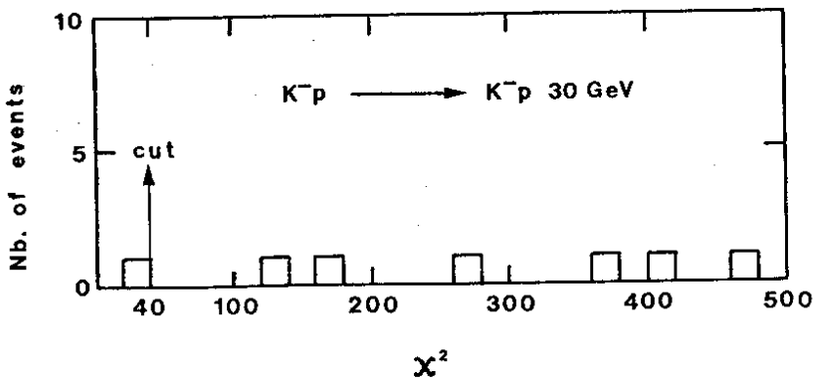

Fig. 9b

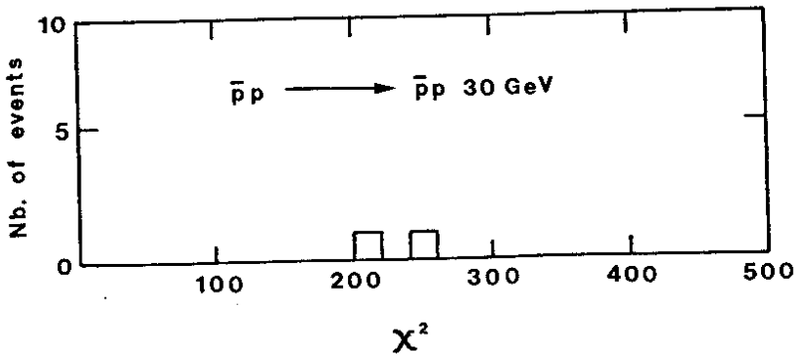

Fig. 9c

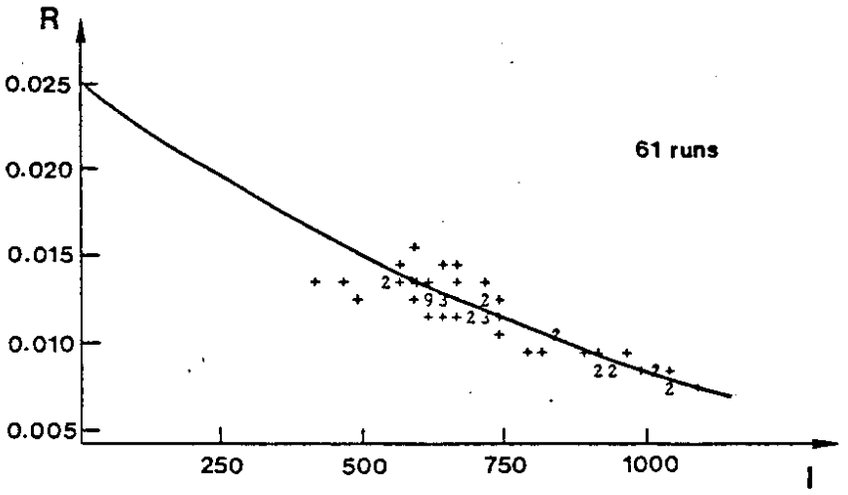

Fig. 10

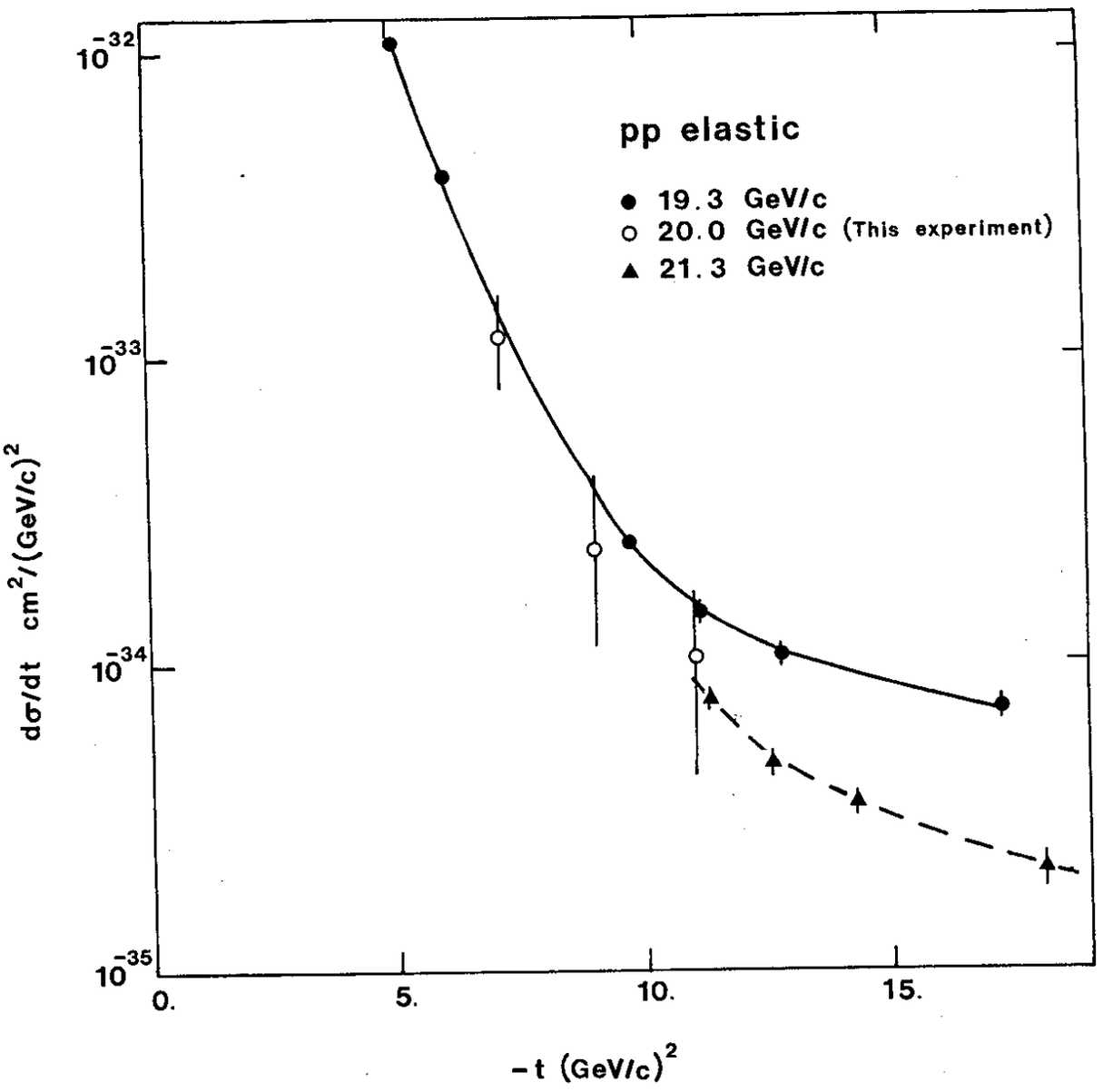
pp elastic
● 19.3 GeV/c
○ 20.0 GeV/c (This experiment)
▲ 21.3 GeV/c
10^{-32}
10^{-33}
10^{-34}
10^{-35}
0.
5.
10.
15.
$d\sigma/dt$ $cm^2/(GeV/c)^2$
$-t$ $(GeV/c)^2$

Fig. 11

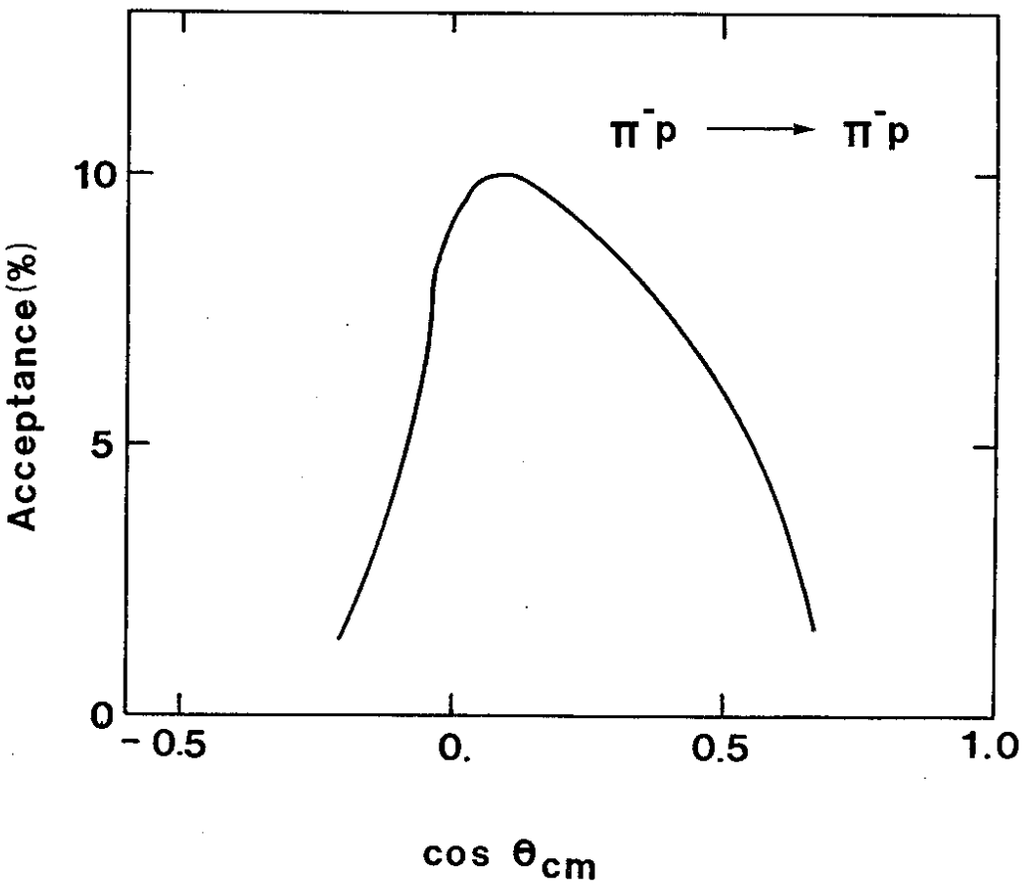

Fig. 12a

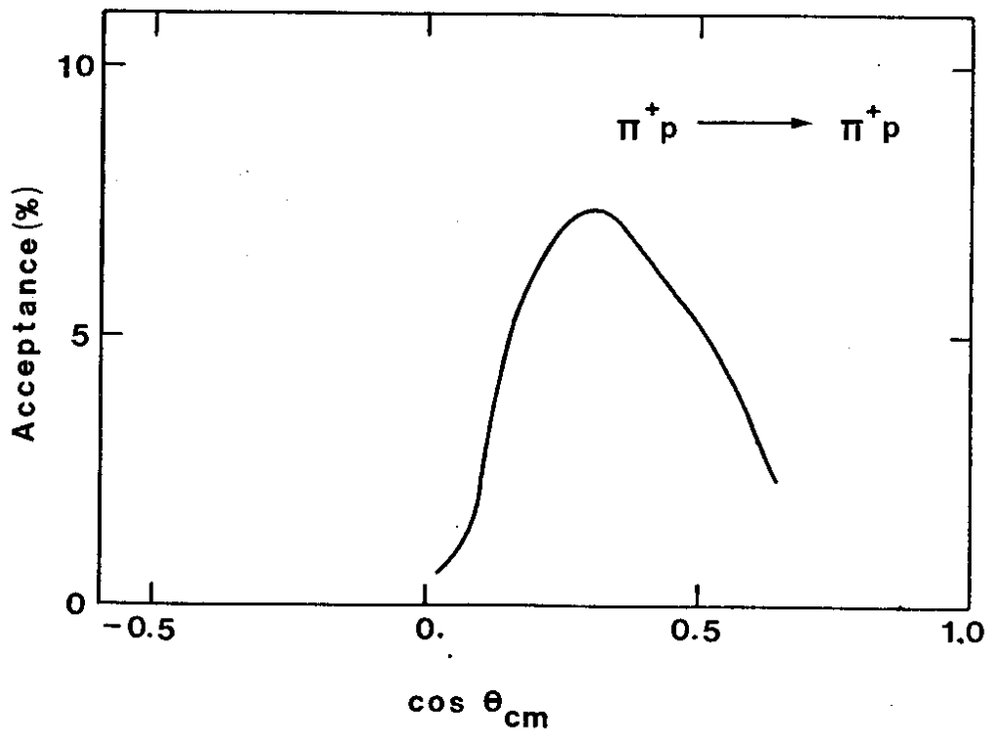

Fig. 12b

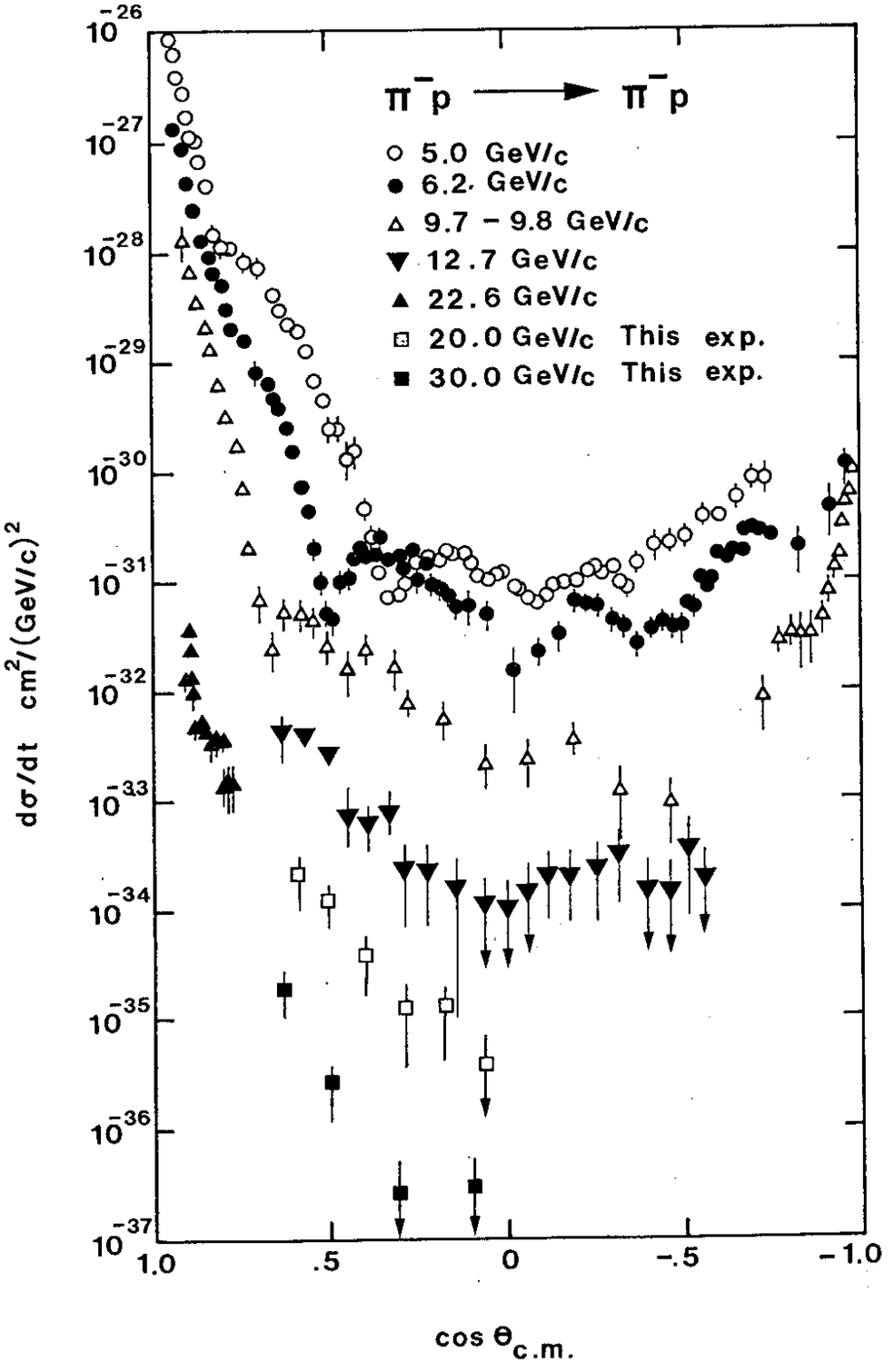
$\pi^- p \longrightarrow \pi^- p$
5.0 GeV/c
6.2 GeV/c
9.7 – 9.8 GeV/c
12.7 GeV/c
22.6 GeV/c
20.0 GeV/c This exp.
30.0 GeV/c This exp.
$d\sigma/dt$ cm^2/(GeV/c)^2
10^{-26}
10^{-27}
10^{-28}
10^{-29}
10^{-30}
10^{-31}
10^{-32}
10^{-33}
10^{-34}
10^{-35}
10^{-36}
10^{-37}
1.0
.5
0
-.5
-1.0
cos $\theta_{c.m.}$

Fig. 13

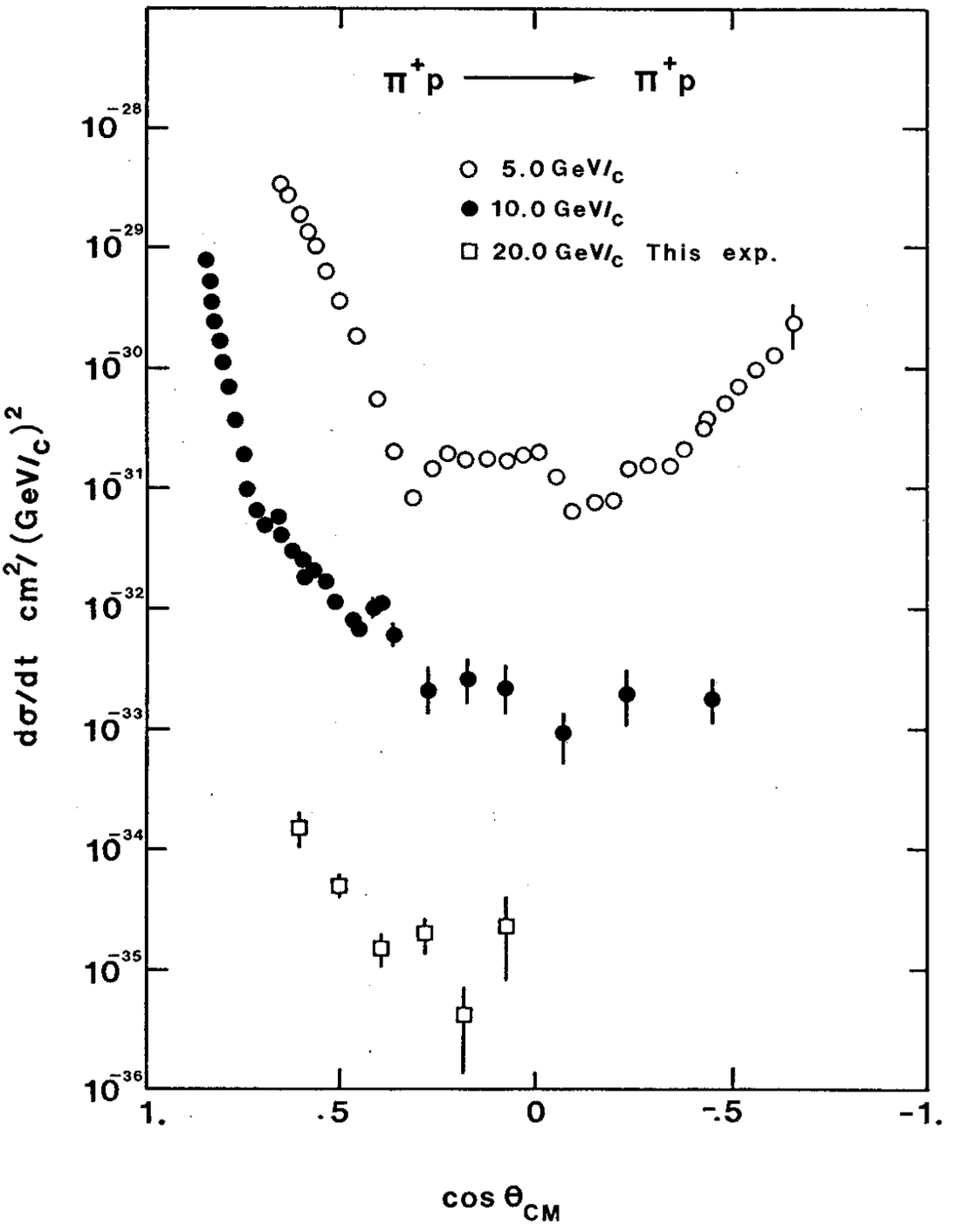
$\pi^+ p \longrightarrow \pi^+ p$
5.0 GeV/c
10.0 GeV/c
20.0 GeV/c This exp.
$d\sigma/dt$ cm^2/(GeV/c)^2
10^{-28}
10^{-29}
10^{-30}
10^{-31}
10^{-32}
10^{-33}
10^{-34}
10^{-35}
10^{-36}
1.
.5
0
-.5
-1.
cos θ_{CM}

Fig. 14

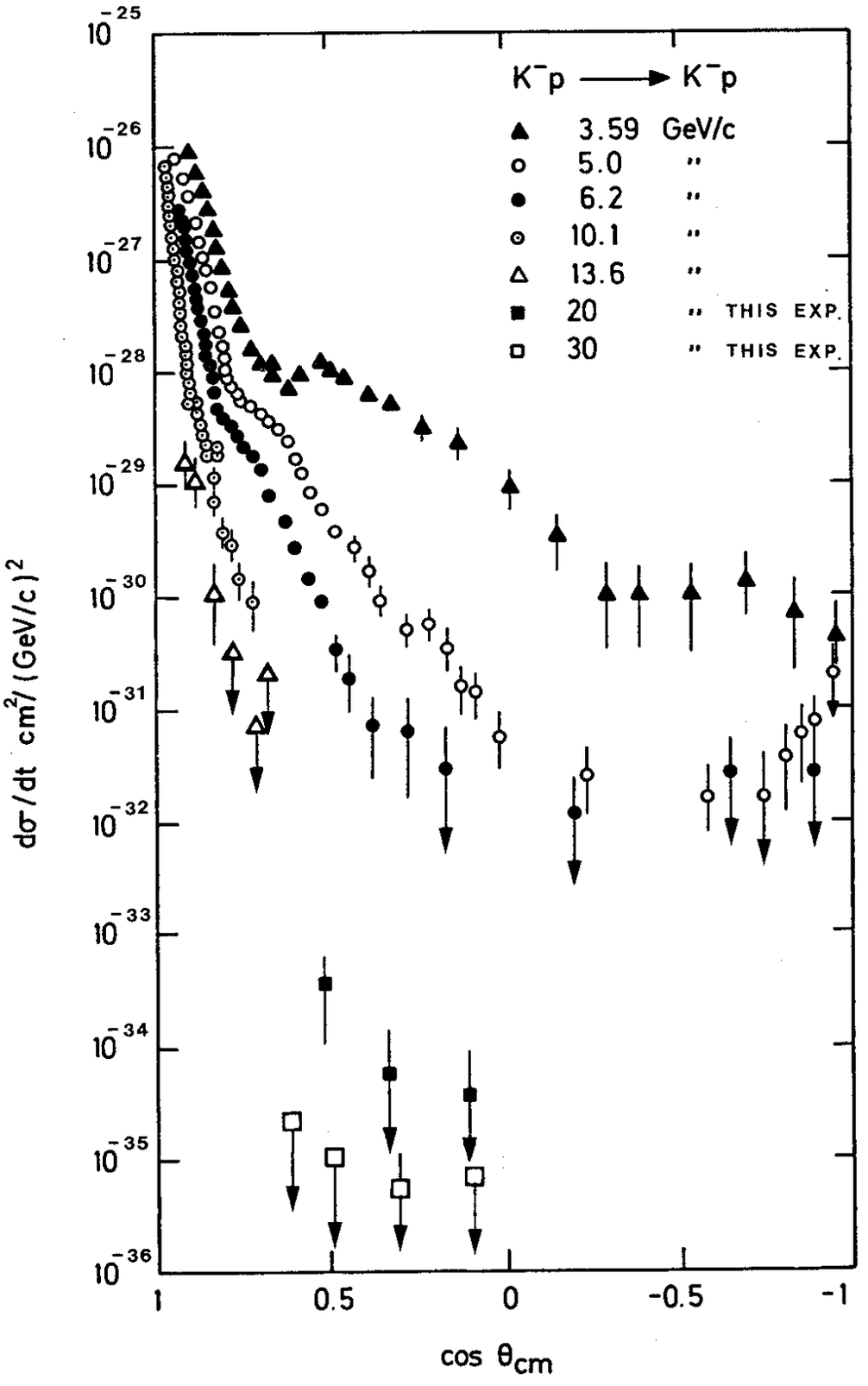
$K^-p \longrightarrow K^-p$
3.59 GeV/c
5.0 "
6.2 "
10.1 "
13.6 "
20 " THIS EXP.
30 " THIS EXP.
$d\sigma/dt$ cm^2/ (GeV/c)^2
10^{-25}
10^{-26}
10^{-27}
10^{-28}
10^{-29}
10^{-30}
10^{-31}
10^{-32}
10^{-33}
10^{-34}
10^{-35}
10^{-36}
1
0.5
0
-0.5
-1
cos θ_{cm}

Fig. 15

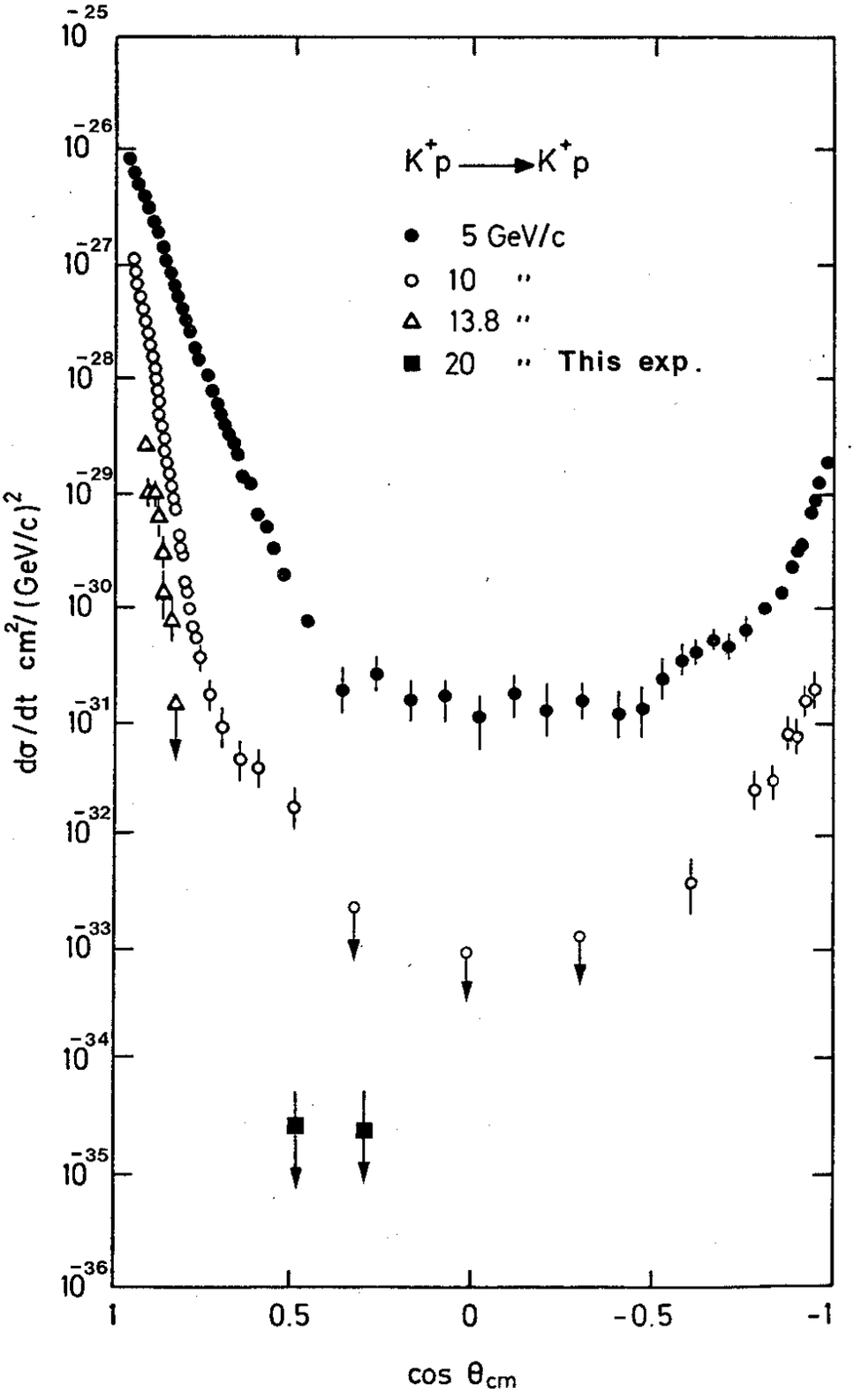
$K^+p \longrightarrow K^+p$
5 GeV/c
10 "
13.8 "
20 " This exp.
$d\sigma/dt$ cm^2/(GeV/c)^2
10^{-25}
10^{-26}
10^{-27}
10^{-28}
10^{-29}
10^{-30}
10^{-31}
10^{-32}
10^{-33}
10^{-34}
10^{-35}
10^{-36}
1
0.5
0
-0.5
-1
cos θ_{cm}

Fig. 16

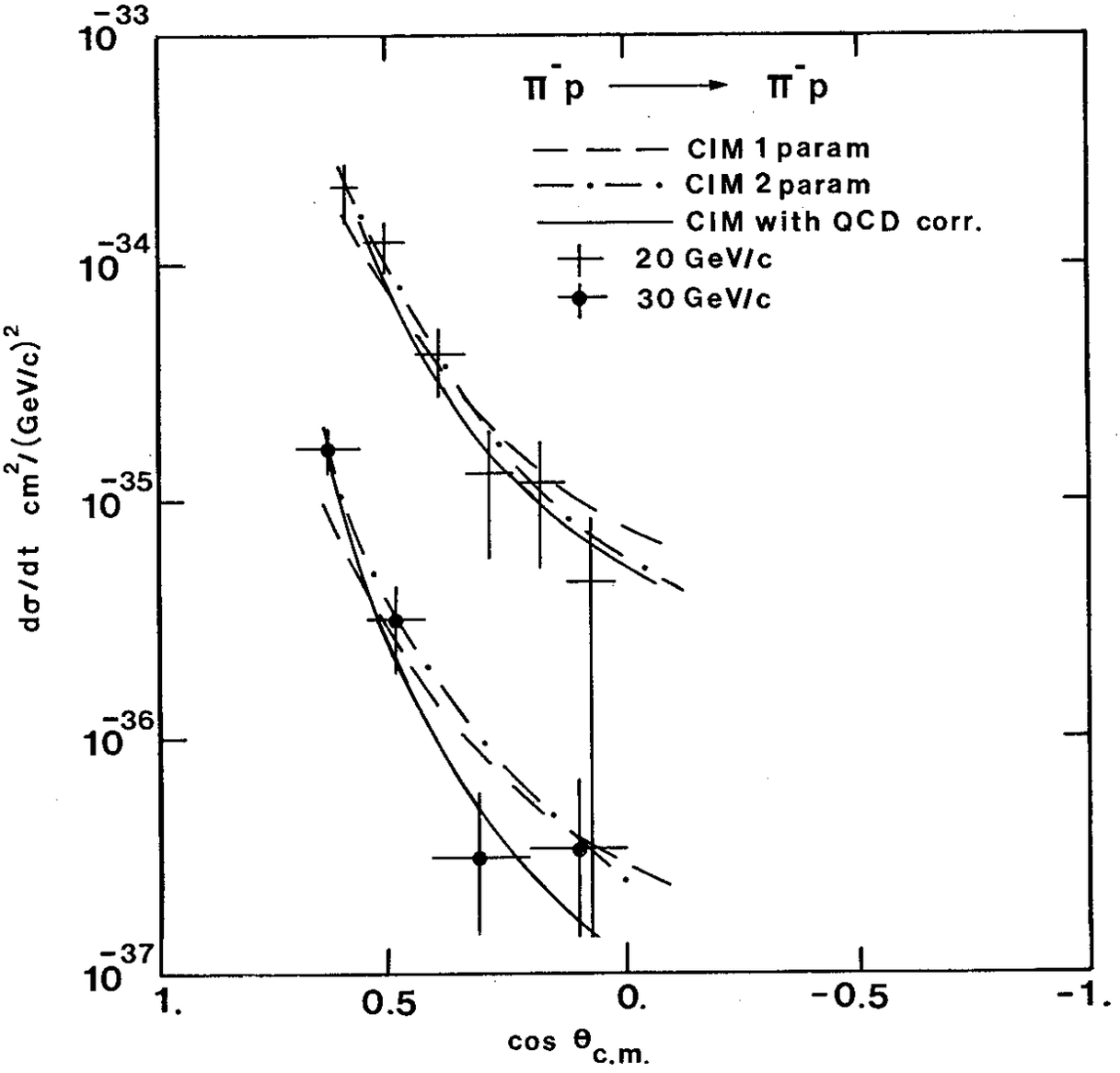
$\pi^- p \longrightarrow \pi^- p$
CIM 1 param
CIM 2 param
CIM with QCD corr.
20 GeV/c
30 GeV/c
$d\sigma/dt$ cm^2/(GeV/c)^2
10^{-33}
10^{-34}
10^{-35}
10^{-36}
10^{-37}
1.
0.5
0.
-0.5
-1.
cos $\theta_{c.m.}$

Fig. 17

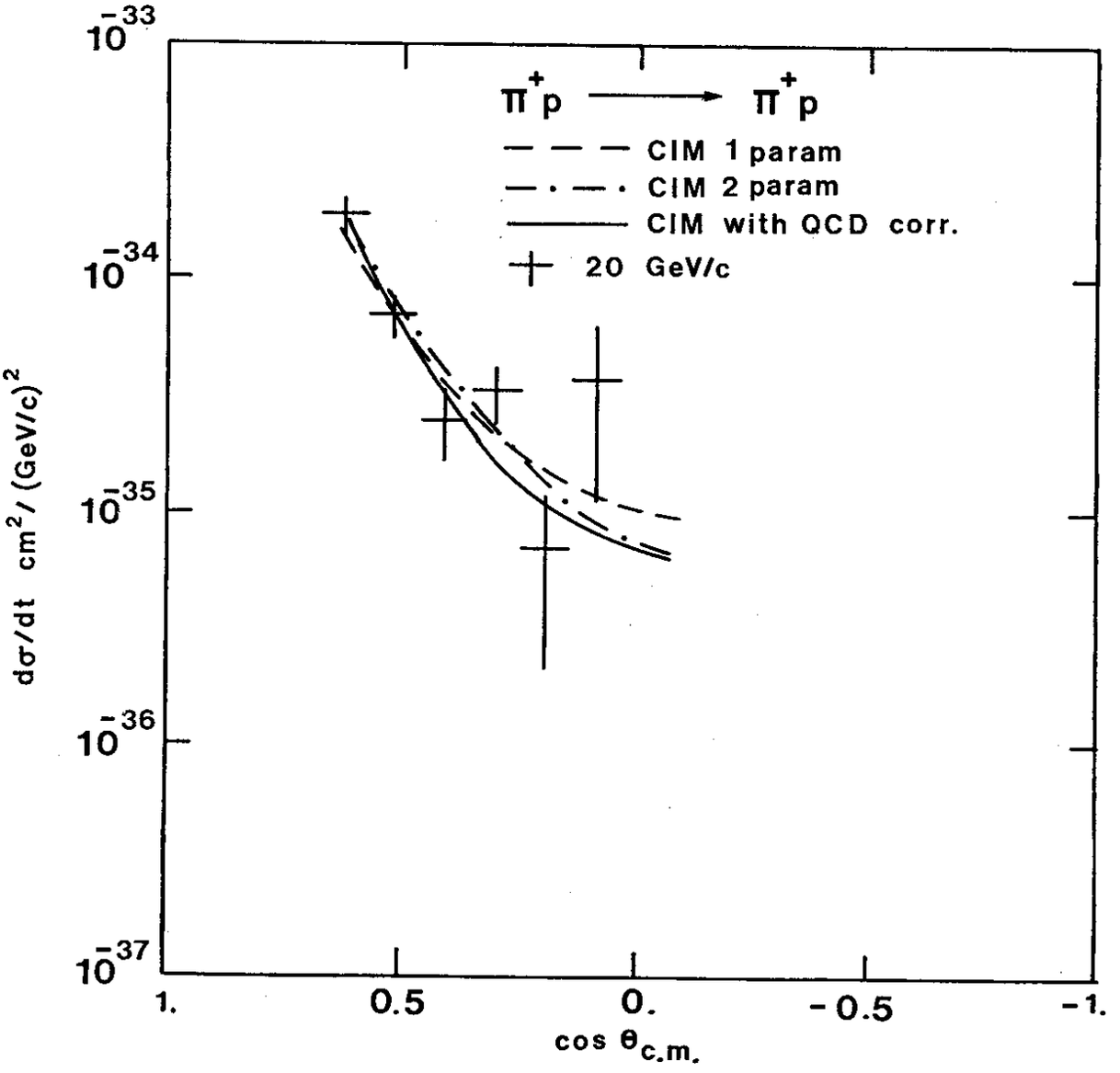
$\pi^+ p \longrightarrow \pi^+ p$
CIM 1 param
CIM 2 param
CIM with QCD corr.
20 GeV/c
10^{-33}
10^{-34}
10^{-35}
10^{-36}
10^{-37}
$d\sigma/dt$ cm^2/ (GeV/c)^2
1.
0.5
0.
-0.5
-1.
cos $\theta_{c.m.}$

Fig. 18

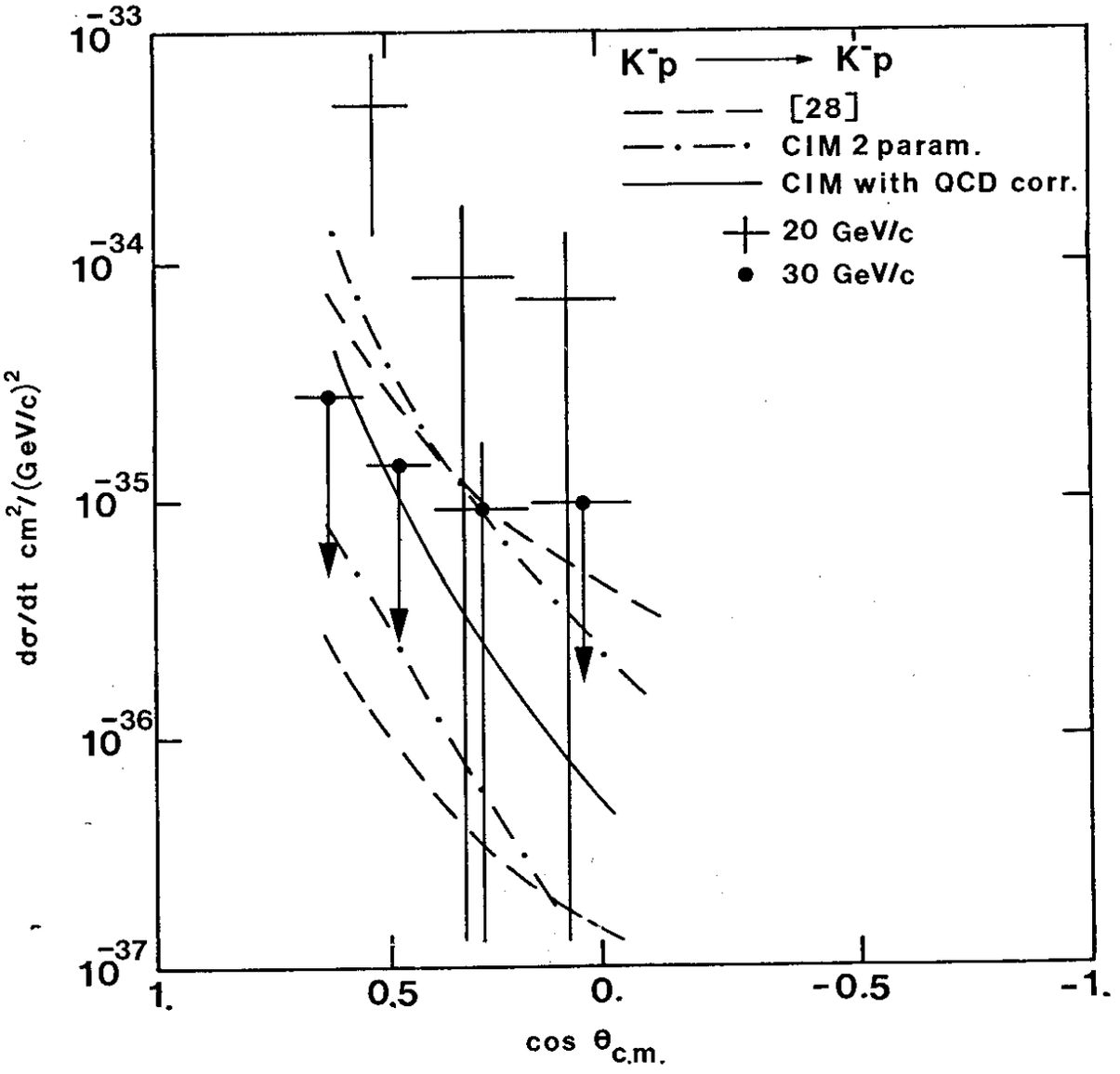
$K^-p \longrightarrow K^-p$
[28]
CIM 2 param.
CIM with QCD corr.
20 GeV/c
30 GeV/c
$d\sigma/dt$ cm^2/(GeV/c)^2
10^{-33}
10^{-34}
10^{-35}
10^{-36}
10^{-37}
1.
0.5
0.
-0.5
-1.
cos $\theta_{c.m.}$

Fig. 19

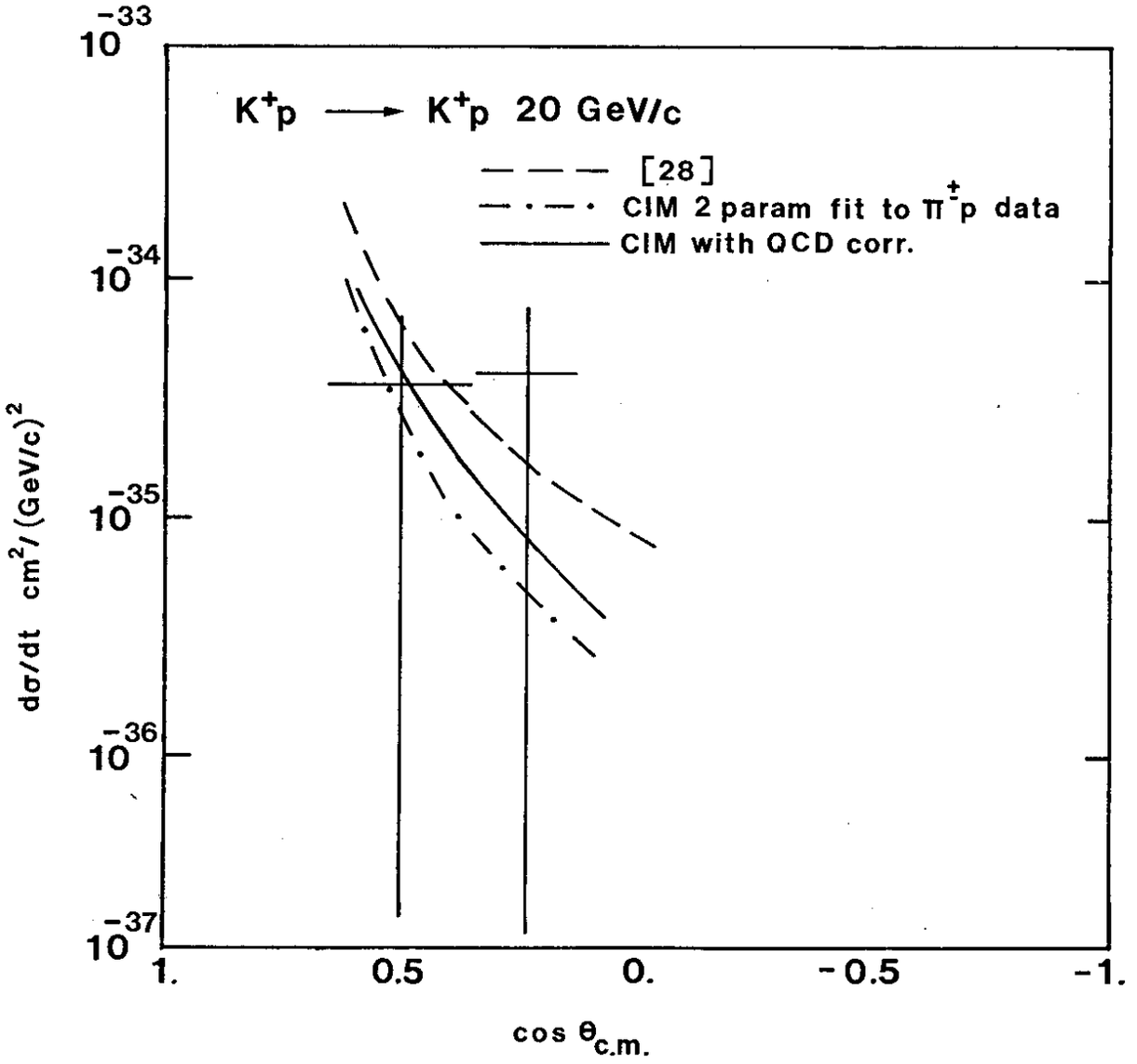
$K^+p \longrightarrow K^+p$ 20 GeV/c
[28]
CIM 2 param fit to $\pi^{\pm}p$ data
CIM with QCD corr.
$d\sigma/dt$ cm^2/(GeV/c)^2
10^{-33}
10^{-34}
10^{-35}
10^{-36}
10^{-37}
1.
0.5
0.
-0.5
-1.
cos $\theta_{c.m.}$

Fig. 20

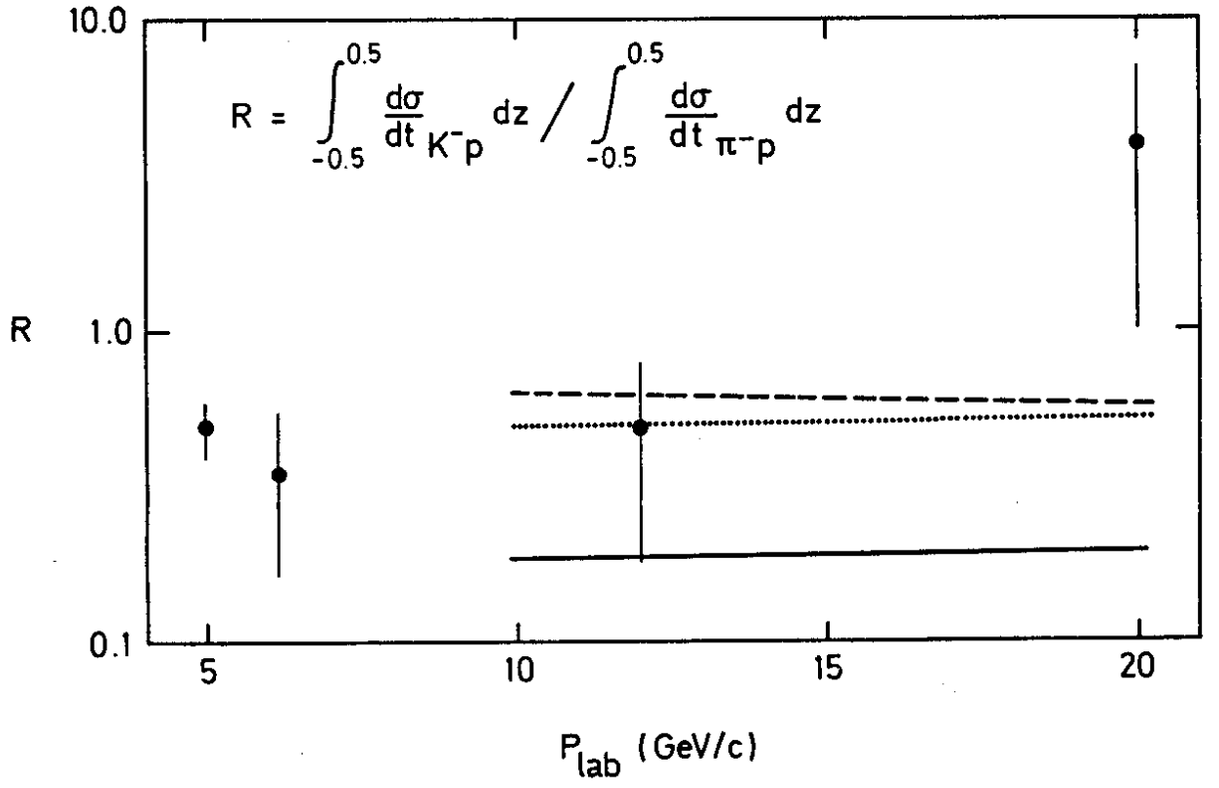
10.0
1.0
0.1
R
$R = \int_{-0.5}^{0.5} \frac{d\sigma}{dt}_{K^-p} dz \Big/ \int_{-0.5}^{0.5} \frac{d\sigma}{dt}_{\pi^-p} dz$
5
10
15
20
P_{lab} (GeV/c)

Fig. 21

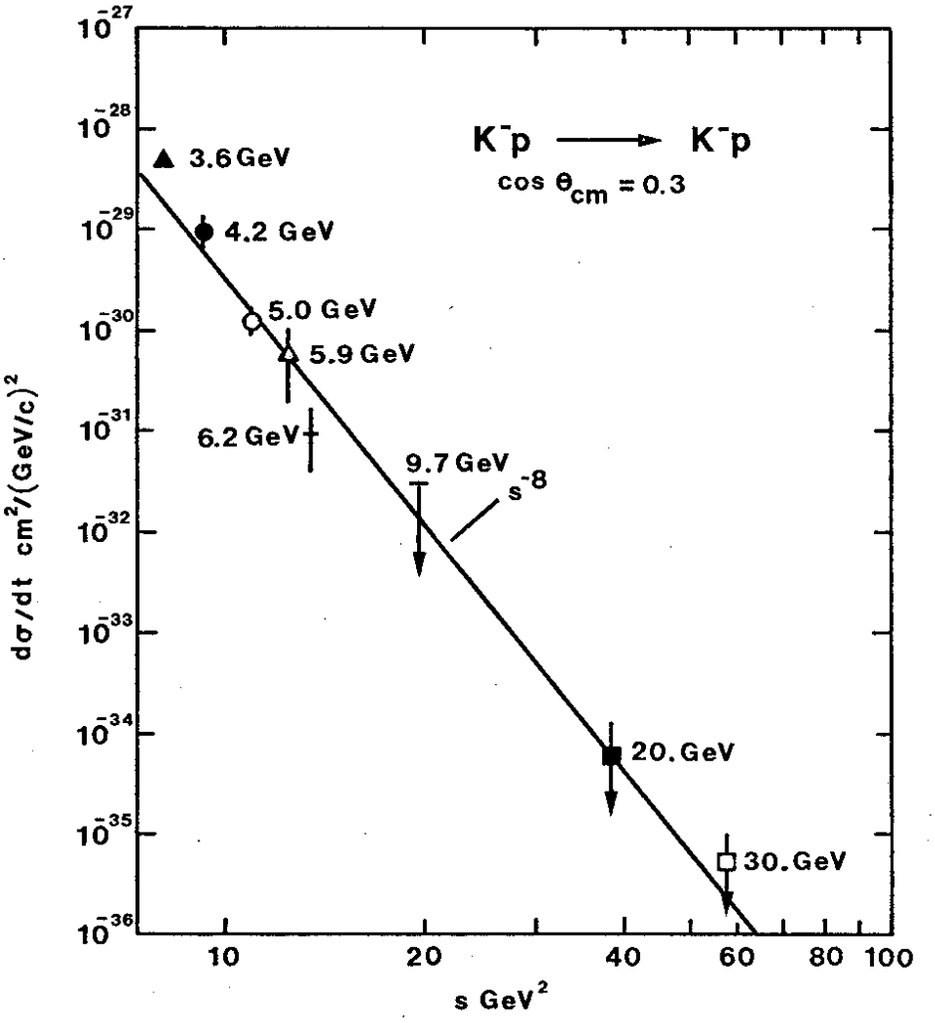
$K^-p \longrightarrow K^-p$
$\cos\theta_{cm} = 0.3$
3.6 GeV
4.2 GeV
5.0 GeV
5.9 GeV
6.2 GeV
9.7 GeV
s^{-8}
20. GeV
30. GeV
$d\sigma/dt$ cm^2/(GeV/c)^2
s GeV^2
10^{-27}
10^{-28}
10^{-29}
10^{-30}
10^{-31}
10^{-32}
10^{-33}
10^{-34}
10^{-35}
10^{-36}
10
20
40
60
80
100

Fig. 22

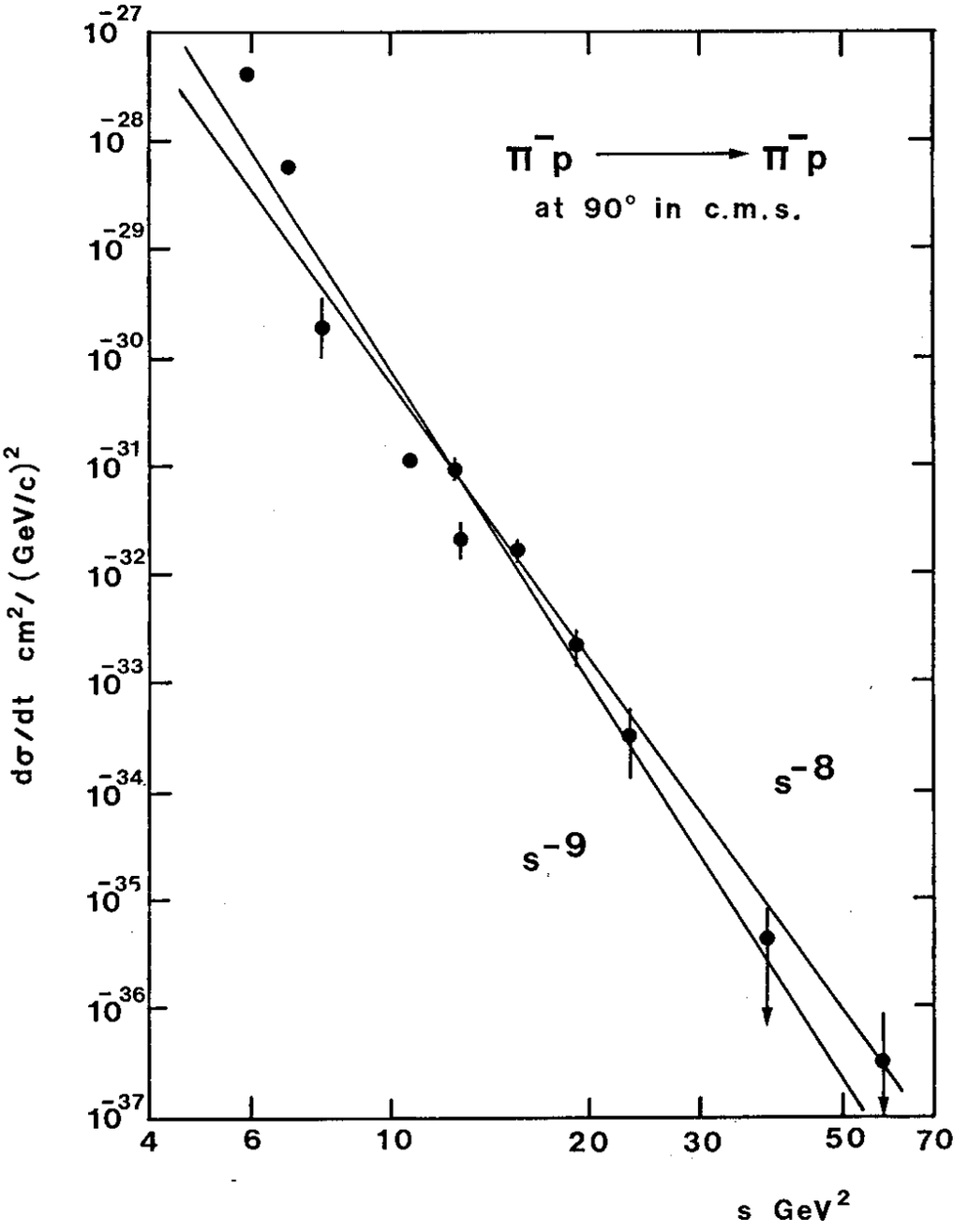
$\pi^- p \longrightarrow \pi^- p$
at 90° in c.m.s.
s^{-8}
s^{-9}
$d\sigma/dt$ cm^2/(GeV/c)^2
s GeV^2
10^{-27}
10^{-28}
10^{-29}
10^{-30}
10^{-31}
10^{-32}
10^{-33}
10^{-34}
10^{-35}
10^{-36}
10^{-37}
4
6
10
20
30
50
70

Fig. 23